

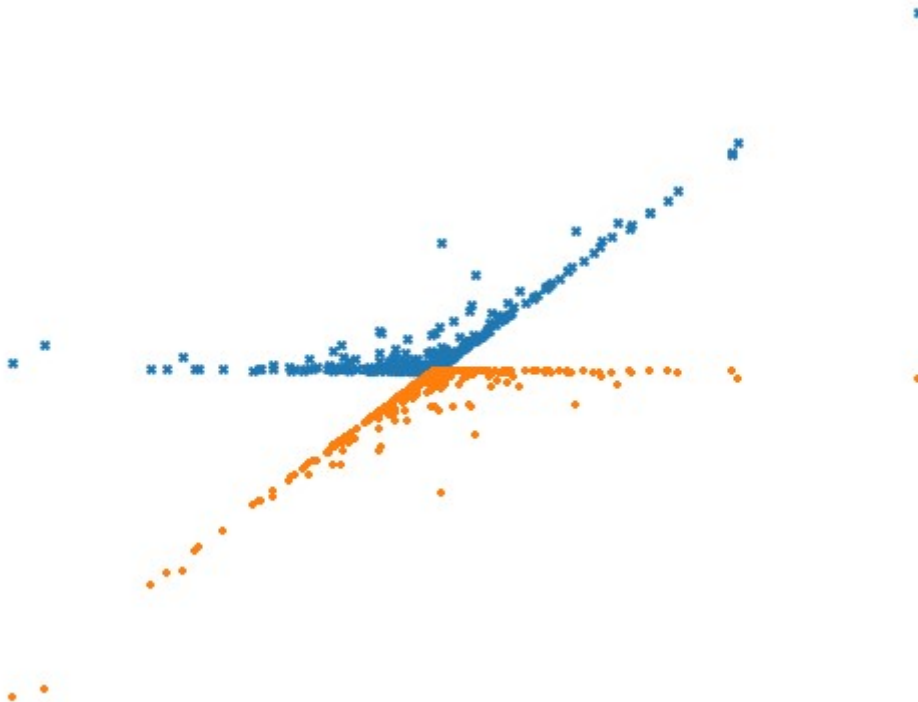
Degree Project in Space Technology

Second Cycle, 30 credits

Risk Assessment for Space Debris Collisions

Creating a Combined Fragmentation and Risk Model to Assess the Risk of In-orbit Fragmentation Events

KENNY ANDERSSON



Author

Kenny Andersson, kenny@kth.se
M.Sc. Aerospace Engineering.
Royal Institute of Technology (KTH)

Location

Swedish Defence Research Agency (FOI)
Stockholm, Sweden

Examiner

Gunnar Tibert
Department of Engineering Mechanics,
Royal Institute of Technology (KTH)
Stockholm, Sweden

Supervisors

Torbjörn Sundberg
Swedish Defence Research Agency (FOI)
Stockholm, Sweden

Gunnar Tibert
Department of Engineering Mechanics,
Royal Institute of Technology (KTH)
Stockholm, Sweden

Abstract

The increasing reliance on space infrastructure and its rapid expansion necessitate the development and enhancement of tools for space debris and fragmentation research. Accurate prediction of the risks associated with satellite fragmentation requires comprehensive understanding of the dynamics involved. To address this need, the widely used NASA Standard Breakup Model (SBM) is employed in this thesis to predict fragment characteristics resulting from breakup events. Additionally, a novel method is introduced to determine the direction of these fragments, something not directly covered by the SBM. Furthermore, the principle of kinetic gas theory is applied to calculate the overall, long-term collision risk between debris and a predetermined satellite population. The results from this reveal the limitations of the SBM in accurately simulating fragmentations for certain satellite types. However, the newly implemented fragment directionality method aligns well with observed data, suggesting its potential for further research. Similarly, the risk model exhibits strong correspondence with ESA's MASTER, a model used for assessing collision risks with debris, with the deviations likely due to different impact velocity models used. Finally, the validated fragmentation and risk models are combined, and the combined model is used to analyse a real-world fragmentation event.

Keywords

space debris; NASA standard breakup model; satellite fragmentations; satellite fragmentation modelling; space surveillance and tracking; ESA MASTER; collision risk; risk assessment; space situational awareness

Sammanfattning

Det ökande beroendet av rymdinfrastruktur, samt dess snabba expansion kräver utveckling och förbättring av verktyg för forskning och analys kring rymdskräp och fragmentering. För att förstå risken förknippad med satellitfragmentationer så krävs förståelse för den involverade dynamiken. För att tillgodose detta används NASA:s Standard Breakup Model (SBM) i denna avhandling för att bestämma fragmentegenskaper som bildas från olika sorters fragmentationshändelser. Dessutom introduceras en ny metod för att bestämma riktningen för dessa fragment, något som inte direkt täcks av SBM. Dessutom tillämpas principen för kinetisk gasteori för att beräkna den totala, långsiktiga kollisionsrisken mellan rymdskrot och en förutbestämd satellitpopulation. Resultaten från detta avslöjar SBM:s begränsningar när det gäller att simulera fragmenten för vissa satellittyper. Hursomhelst så kan man se att den nyligen implementerade fragmentriktningsmetoden stämmer väl överens med den observerade datan, vilket tyder på dess potential för ytterligare forskning. På samma sätt uppvisar riskmodellen överensstämmelse med ESA:s MASTER, en modell som används för att bedöma kollisionsrisker med rymdskrot, där avvikelser sannolikt beror på att olika kollisionshastighetmodeller används. Slutligen kombineras de validerade fragmenterings- och riskmodellerna, som sedan används för att bidra med analyser till en riktig fragmentationshändelse.

Nyckelord

rymdskrot; NASA standard breakup model; satellitfragmentering; modellering av satellitfragmentering; inmätning och övervakning av rymdobjekt; ESA MASTER; kollisionsrisk; riskbedömning; rymdlägesbild

Acknowledgements

I would like to express my heartfelt gratitude to my supervisor at FOI, Torbjörn Sundberg. His invaluable guidance, and wealth of insights have been instrumental in shaping this thesis and reaching my conclusions. This appreciation extends to all my colleagues at FOI. Not only have they been a wonderful source of assistance, but have also made the workplace an incredibly enjoyable and stimulating environment.

Furthermore, I would like to express a special thank you to my roommates at FOI, Mathias Dahlman, Erik Jonsäll, and Emma Mattson. Their continuous support and friendship have made a significant difference.

Finally, I would like to thank my professor and examiner Gunnar Tibert for his guidance and help throughout my Master's education at KTH.

Kenny Andersson

June 2023, Stockholm

Acronyms

LEO	Low Earth Orbit
ASAT	Anti-satellite weapon
ESA	European Space Agency
DIS-COS	Database and Information System Characterising Objects in Space
NASA	National Aeronautics and Space Administration
SBM	Standard Breakup Model
ISS	International Space Station
SST	Space Surveillance and Tracking
FOI	Totalförsvarets Forskninginstitut (Swedish Defence Research Agency)
ECI	Earth-centered inertial
RAAN	Right ascension of the ascending node
SSO	Sun-synchronous orbit
TLE	Two-line element set
MASTER	Meteoroid and Space Debris Terrestrial Environment Reference
PDF	Probability distribution function
SSN	Space Surveillance Network
RB	Rocket body
SC	Spacecraft
SOCIT	Satellite Orbital Debris Characterization Impact Tests
SLSQP	Sequential Least Squares Programming

List of Symbols

G	Universal gravitational constant
μ	Standard gravitational parameter
P	Orbital period
a	Semi-major axis
e	Eccentricity
i	Inclination
Ω	Longitude of ascending node
ω	Argument of periapsis
ν	True anomaly
r	Orbital distance
r_A	Apoapsis
r_P	Periapsis
C_D	Drag coefficient
\mathbf{v}	Velocity
\mathbf{F}	Force
m	Mass of satellite
M	Mass of parent body
ρ	Atmospheric density
E	Energy
R_\oplus	Earth radius
n	Mean motion
u	Argument of latitude
ξ	Plane change angle
λ	Latitude
F	Flux
S	Spatial density
Δv_i	Impact velocity
P_{coll}	Collision probability
σ	Cross-sectional area
L_c	Characteristic length
A/M	Area-to-mass ratio
$\mathcal{N}(\cdot, \cdot)$	Normal distribution
θ	Rotation angle
P_l	l th Legendre polynomial

List of Figures

1.1	Plot showing the number of objects orbiting the Earth [3].	1
2.1	Orbital elements of an object orbiting a central body centered at the origin.	7
2.2	Illustration of apsidal precession of an elliptical orbit.	10
2.3	Gabbard diagram of a simulated explosion of an upper stage orbiting in a near-circular 600 km orbit.	12
2.4	Gabbard diagram of a simulated explosion of an upper stage orbiting in an elliptical 9600 by 2400 km altitude orbit.	13
2.5	Gabbard Diagram of the fragments created by the 2007 Fengyun-1C ASAT test, with data obtained from space-track.org [16]. The ‘claw’ shape that appears due to drag can be seen on the left ‘forbidden region’, and shows that many of the fragments used in this plot were observed a long time after fragmentation [1].	16
2.6	Velocity diagrams of the Fengyun-1C ASAT test showing direction of impact [12], as well as number of objects in each quadrant. Data obtained from space-track.org [16].	17
2.7	Illustration of how the relative velocity between a cloud of particles and an object effects the flux of particles through the object.	18
2.8	Spatial density of debris larger than 5 cm vs. altitude above Earth’s surface. The Geostationary belt can be seen to the far right as a very small peak. The horizontal axis is in log-scale. Data obtained from ESA’s MASTER for the time period 2016-11-01 [28].	19
2.9	Spatial density of debris larger than 5 cm vs. altitude above Earth’s surface and declination. The SSO is clearly visible as two peaks. The vertical axis is in log-scale. Data obtained from ESA’s MASTER for the time period 2016-11-01 [28].	19
2.10	Impact velocity PDF for an object at an altitude of 400 km, with an inclination of 30°.	20
3.1	Flow diagram of how each model is used to generate a collision probability. The circles represents inputs/outputs, and the boxes represents the various models used in the process.	26
3.2	Depiction of the different possible solutions to the optimization problem. The left image is the direct solution from scipy’s SLSQP algorithm, whereas the right image is a solution from the Monte Carlo algorithm. Each point represents the change in velocity of a fragment.	30
3.3	Flow diagram of the breakup model used in this thesis.	31

3.4	Illustration of what a bin used for calculating spatial densities looks like. For the purpose of this thesis $d\phi$ is 2π , thereby causing the differential volume to form a torus-like shape. The center of the coordinate system corresponds to the center of the Earth.	33
4.1	Gabbard diagram of the NOAA-3 Delta 1 upper stage explosion (left), as well as the simulated Gabbard diagram from the model (right). . . .	37
4.2	Velocity perturbations of the NOAA-3 Delta 1 upper stage explosion (blue), as well as the simulated results from the model (orange). The numbers indicate the number of fragments on each octant, on the format: Data Simulated.	37
4.3	Velocity perturbation histograms of the NOAA-3 Delta 1 upper stage explosion (blue), as well as the simulated results from the model (orange). The numbers indicate the number of fragments on each half, on the format: Data Simulated.	38
4.4	Normalized velocity perturbation histograms of the NOAA-3 Delta 1 upper stage explosion (blue), as well as the simulated results from the model (orange). The numbers indicate the number of fragments on each half, on the format: Data Simulated.	38
4.5	Gabbard diagram of the NOAA-16 explosion (left), as well as the simulated Gabbard diagram from the model (right).	39
4.6	Velocity perturbations of the NOAA-16 explosion (blue), as well as the simulated results from the model (orange). The numbers indicate the number of fragments on each octant, on the format: Data Simulated.	40
4.7	Velocity perturbation histograms of the NOAA-16 explosion (blue), as well as the simulated results from the model (orange). The numbers indicate the number of fragments on each half, on the format: Data Simulated.	40
4.8	Normalized velocity perturbation histograms of the NOAA-16 explosion (blue), as well as the simulated results from the model (orange). The numbers indicate the number of fragments on each half, on the format: Data Simulated.	41
4.9	Plots showing the Gabbard diagram of Iridium-33 (left), as well as the simulated results from the model (right).	42
4.10	Velocity perturbations of Iridium-33 (blue), as well as the simulated results from the model (orange). The numbers indicate the number of fragments on each octant, on the format: Data Simulated.	42
4.11	Velocity perturbation histograms of Iridium-33 (blue), as well as the simulated results from the model (orange). The numbers indicate the number of fragments on each half, on the format: Data Simulated.	43
4.12	Normalized velocity perturbation histograms of Iridium-33 (blue), as well as the simulated results from the model (orange). The numbers indicate the number of fragments on each half, on the format: Data Simulated.	43
4.13	Gabbard diagram of Cosmos-2251 (left), as well as the simulated Gabbard diagram from the model (right).	44

4.14	Velocity perturbations of Cosmos-2251 for both ascending and descending modes. The number of fragments in each quadrant is also specified in the format ascending descending (left). The simulated results from the model are also shown (right).	44
4.15	Velocity perturbation histograms of Cosmos-2251 (left), as well as the simulated results from the model (right).	44
4.16	Density of operational satellites for different declinations and altitudes. The figure to the right is a zoomed view of LEO. Note that the colour bar is in log scale.	46
4.17	Collision probability of a spacecraft with another functioning spacecraft with the orbital parameters shown in the axes, an inclination of 0° , and a cross-sectional area of 75 m^2 , for a mission duration of 14 years (assuming constant density). Note that the colour bar is in log scale. .	46
4.18	The explosion that generates the highest collision risk with other functioning satellites. The position of the explosion is marked with a red star, and the blue lines are the fragment's trajectories.	49
B.1	Illustration of the meanings of different variables, based on Figure 8.3 in [18].	65

List of Tables

2.1	Table containing the values of S in (2.46) for different cases [33].	23
3.1	Orbital parameters of the Iridium-33 and Cosmos-2251 satellites, prior to collision, as well as the NOAA-3 Delta upper stage, and the NOAA-16 satellite prior to explosion [23].	35
3.2	Parameters used when verifying the flux model.	35
4.1	Flux [$\text{m}^{-2} \text{y}^{-1}$] for the orbits specified in Table 3.2, using a spatial density containing debris larger than 1, 5, and 10 cm, using the analytical and simulated impact velocity model. The ratio between the model values and the MASTER value is also provided to facilitate comparisons.	45
4.2	10 year collision probabilities for the orbits specified in Table 3.2, using a spatial density containing debris larger than 1, 5, and 10 cm, for a spacecraft with a surface area of 75 m^2 , using the analytical and simulated impact velocity model. The ratio between the model value and the MASTER value is also provided to facilitate comparisons. . . .	47
4.3	Variables and their ranges used for the fragmentation and collision risk test. The notations used are the same as in Section 2.1.1.	48
4.4	Collision risk of simulated debris from the NOAA-16 explosion.	50
4.5	Collision risk of simulated debris from the NOAA-16 explosion, divided into groups based on detection probability.	50
A.1	Table describing the different fields of the TLE [16].	63

Contents

1	Introduction	1
1.1	Problem and Objective	4
1.1.1	Objectives	4
1.1.2	Problem identification	4
1.1.3	Delimitations	5
1.1.4	The Swedish Defence Research Agency (FOI)	5
2	Theory	6
2.1	Theoretical Background	6
2.1.1	Orbital mechanics	6
2.1.2	Fragmentation theory	10
2.1.3	Velocity perturbations of debris	13
2.1.4	Section summary	15
2.2	Risk Analysis	17
2.3	Models	20
2.3.1	ESA’s MASTER tool	21
2.3.2	NASA’s Standard Breakup Model	21
3	Method	26
3.1	Breakup Model	26
3.1.1	Mass conservation	26
3.2	Fragment Velocity Model	27
3.2.1	Implementing the model	30
3.3	Spatial Density Model	31
3.3.1	MASTER	32
3.3.2	TLE data	32
3.4	Collision Probability Implementation	33
3.5	Model Verification	34
3.5.1	Verifying the breakup model	34
3.5.2	Verifying the collision probability model	35
4	Results	36
4.1	Breakup Model Results	36
4.1.1	Validation	36
4.2	Spatial Density Model Results	45
4.3	Risk Assessment Results	46
4.4	Obtaining the Results	47
5	Discussion	51

5.1	Breakup Model	51
5.2	Risk Model	54
5.3	Combined Model	55
6	Conclusion	57
6.1	Future Work	58
	Bibliography	59

Chapter 1

Introduction

The interest in space is rapidly increasing, both in the commercial and non-commercial sectors with companies such as SpaceX aiming to launch thousands of satellites into an already crowded Low Earth Orbit (LEO). As space becomes a bigger part of our day-to-day life, it becomes increasingly important to keep it safe and accessible.

Today there are more satellites in space than ever, with thousands more planned in the so-called *mega-constellations* such as SpaceX's StarLink, Amazon's Kuiper and OneWeb. Each of these constellations has the risk of drastically altering the space environment. There are many cases of satellites colliding or spontaneously exploding in orbit due to battery faults or leftover fuel (see for example NOAA-16 [1]), and several countries have shown the capability to target satellites with anti-satellite weapons (ASATs) [1]. Both of these cases have the risk of creating a significant amount of debris, clearly seen in Figure 1.1. Each piece of debris can cause unrecoverable damage to other satellites, which in turn might lead to a cascading effect, called the *Kessler Syndrome* [2].

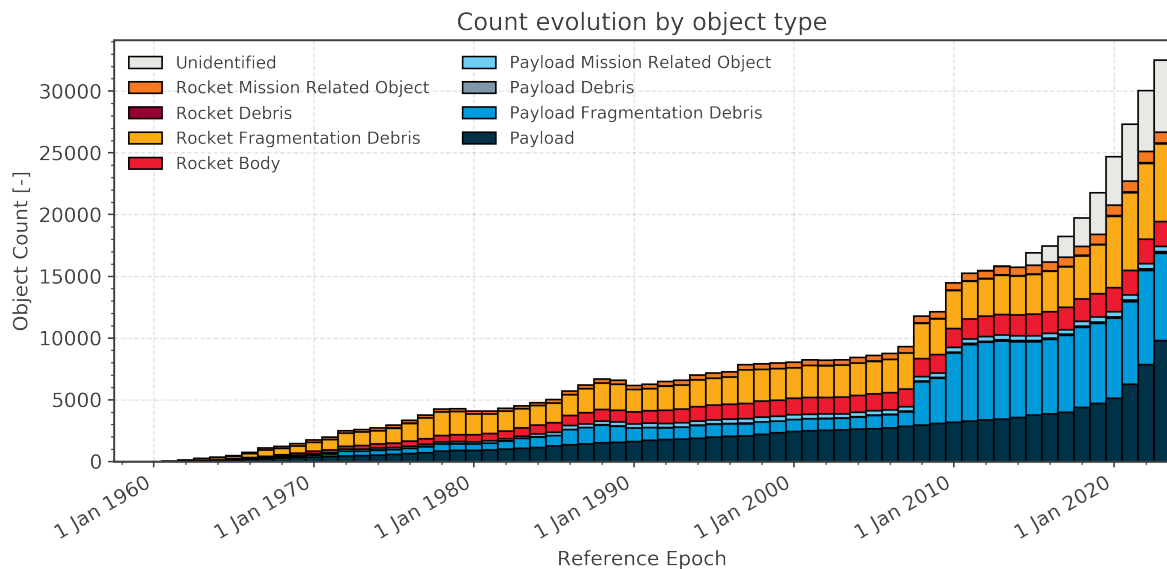


Figure 1.1: Plot showing the number of objects orbiting the Earth [3].

From the start of the space age, hundreds of rocket stages and satellites have fragmented in orbit leaving many thousands trackable pieces of debris that are still orbiting Earth to this day. This, together with spent upper stages, fairings and defunct satellites, pose a threat to everything in orbit. One notable example of this is the collision of the defunct Cosmos-2251 satellite with the operational Iridium-33 satellite in 2009 that created thousands of trackable pieces of debris, of which many are still in orbit [1]. Incidents such as this will become more and more common as the space infrastructure grows. For example, on the 23rd of January 2020, there was a near miss between the defunct satellites IRAS and GGSE-4, with an estimated closest approach of 14 meters and a relative velocity of 15 km/s at an altitude of around 900 km. Had they collided the debris would have stayed in orbit for several decades [4].

Collisions are not the only causes for accidental breakup events. The European Space Agency's (ESA) Database and Information System Characterising Objects in Space (DIS-COS) has characterised nine different types of breakup; including due to propulsion, residual propellant, electrical faults, among others [5]. There are many different cases of these types of fragmentations occurring in orbit, for example the aforementioned NOAA-16 satellite, which in 2015 exploded due to its battery malfunctioning. This is not an isolated incident; the satellite DMSP-F13 also exploded the same year due to a battery malfunction, with even more similar incidents in previous years [1]. Incidents such as these demonstrate the importance of understanding the dynamics of these events. It not only facilitates the ability to determine probable causes, which can reduce the risk of such events happening again in the future, but it also helps reduce the risk for other satellites already in orbit by predicting the debris cloud's propagation. This allows the satellite operators to perform evasive maneuvers, and facilities planning for future operations.

With the advent of military satellites, countries began exploring ways of crippling adversaries' assets using ASATs. In the late 1950s, the United States had already developed a primitive ASAT system called *Bold Orion*, a launch system capable of destroying satellites in LEO using a nuclear warhead [6]. The Soviets were not too far behind, being the first nation to perform extensive tests on real targets [6]. ASAT development continued throughout the 1900s and into the 2000s, with the United States, Russia, India, and China having demonstrated ASAT capabilities on real targets [1, 7]. Each of these tests left significant amounts of debris in orbit, but many of the tests were carried out on satellites in low orbits, such as India's 2019 ASAT test, *Mission Shakti*. This test was carried out on a satellite in a low orbit, such that most of the debris deorbited within a few months, and most of the debris generated was below the orbits of other satellites, thus posing little threat [8]. In contrast, China performed an ASAT test on the Fengyun-1C weather satellite in 2007, which orbited at an altitude of around 860 km. Due to the high energies involved, this test produced the largest number of trackable fragments ever from a single event, including non-ASAT related fragmentations, and due to the high altitude, they will take many decades to deorbit [1]. The debris left by ASAT testing has caused a lot of inconvenience for the space sector, causing more propellant to be spent on evasive maneuvers which may shorten a satellites lifespan. Although only relatively few ASAT tests have been performed compared to other types of fragmentation, debris from these tests constitutes about 11% of all debris in orbit [9].

Both accidental fragmentations and fragmentations due to ASAT tests result in large amounts of debris left in orbit, significantly contributing to the increase in collision risk to other satellites. This is something that has to be incorporated when implementing debris mitigation policies, and as such relevant organizations and agencies develop models to analyze the parameters of interest, such as collision risk and prediction of spread [10]. One of the most used models developed is the National Aeronautics and Space Administration’s (NASA) Standard Breakup Model (SBM).

The SBM describes the breakup of objects in orbit for a variety of different cases, such as collisions of satellites or explosions of upper stages. The model is built using an empirical approach, using data collected from tests on Earth and data from radar observations of debris in space from previous fragmentations to fit the parameters in the model [11].

Taking as input an object’s mass, type, and cause of fragmentation, the SBM generates debris based on distributions. Each piece of debris is given a mass, an area and a velocity, which can then be used in analyses. There are, however, problems with the SBM, notably that it does not conserve mass and the velocity is given as a scalar, not as a vector [11].

The velocity vector distribution is difficult to implement due to it being very dependent on the nature of the fragmentation, such as collision direction and energy, or where on the body an explosion originates from. For example, there are at least three different ways to model an explosion of an upper stage [1]:

- *Clam model*: A rupture in a propellant tank which originates in a single point along the body, thus the fragments mainly disperse in the opposite direction, with some fragments shooting off to the sides.
- *Half-segment model*: Similar to the clam model, but there are two points opposite each other, thus mainly shooting the fragments to the sides.
- *Octant model*: Multiple rupture locations, thus leading to an almost isometric outwards dispersion of fragments.

These models are useful for analyzing the debris generated by an explosion in order to determine its cause, but are less useful for modeling beforehand due to the difficulty of predicting how and where in the spacecraft the explosion will occur. Instead, one can assume that each of the fragments gets a direction evenly distributed along a sphere, which provides a more general case. However, this is inaccurate for collisions, where the fragment distribution may be highly anisotropic [12].

As for collisions, there are many different ways to model them as well; since the collision does not necessarily occur in line with the center-of-mass, or at high enough energies to cause a *catastrophic* collision. The limit when a collision is considered ‘catastrophic’ is usually assumed to be when the energy of the collision exceeds 40 J/g, a number obtained from empirical tests for the SBM [13]. In a catastrophic collision both objects are totally fragmented. Nevertheless, non-catastrophic collisions can still be devastating, especially if it involves a crewed spacecraft. This was seen on the 14th of December 2022 when a micrometeorite or piece of orbital debris collided with the MS-22 Soyuz spacecraft while docked to the International Space Station (ISS), stranding some of the astronauts on board, and causing the spacecraft to leak coolant [14]. The

droplets of coolant may solidify and add to the already high amounts of debris in LEO.

This shows the importance of tracking as much of the existing orbital debris as possible, called Space Surveillance and Tracking (SST), which is often carried out by government agencies such as the U.S. Space Command or European Space Agency (ESA) [15]. The data that the U.S. collects is regularly uploaded on *space-track.org* [16].

1.1 Problem and Objective

The purpose of this study is two-fold. A fragmentation and risk model will be constructed and compared to real-world events in order to see how a potential fragmentation can affect its orbital neighborhood. The model will include a way to simulate a fragmentation, but will also include the tools to determine the spatial densities in space. This model can then be used to calculate how the collision risk may increase for other spacecraft, which can potentially be done by using numerical methods or an analytical approximation to get a relative increase in the probability of collision. The results from this can then be used as a measure to see the long and short term effects of a specific breakup, and possibly determine fragments that pose a larger risk than others which can be targeted by, for example, debris removal missions.

1.1.1 Objectives

The purpose above can be summarized as four main points:

- Evaluate existing fragmentation models to find one that can accurately model various types of fragmentation in space.
- Evaluate the accuracy of the model by comparing it to historic fragmentations.
- Assess the potential consequences and implications of fragmentation events in different orbits, with varying characteristics.
- Evaluate the risk increase from fragmentation events by studying the generated debris and the affected orbits.

The model will be implemented in Python, using preexisting libraries, and tools provided by Totalförsvarets Forskningsinstitut (Swedish Defence Research Agency) (FOI).

1.1.2 Problem identification

Using empirical data to construct a model comes with a few problems. Mainly, the results will be biased towards the properties of the spacecraft that are more likely to suffer a breakup event. For instance, the materials used in satellites are not necessarily consistent between satellites, as well as older satellites, which may be more prone to fragmentation, will cause the data to be biased towards them. Similarly, more spacecraft undergo fragmentations in lower orbits, where the dynamics are different due to, for example, drag. This alters the effects of the fragmentation, which means that higher orbit fragmentations may not be as accurate if modeled using data primarily from lower orbits.

Using data to analyze fragmentations also comes with some limitations. Mainly, many observations are not taken fast enough for orbital perturbations to be negligible, as such corrections due to drag, oblate Earth, and general movement of the debris needs to be taken into account which may affect the quality of the data.

1.1.3 Delimitations

There are many different ways a collision or fragmentation can occur in space, most notably a collision in space may not be in-line with the center of mass, and the energies involved may not be high enough for complete fragmentation. The generated model will be limited to explosions and head-on collisions, whereas observational data can be analyzed for any significant inhomogeneous spread of debris.

Due to the stochastic properties associated with fragmentation models, short-term risk analyses, which rely on propagating fragments to identify potential close encounters, are disregarded as they are unlikely to yield meaningful outcomes. Instead, a long-term risk analysis model based on flux and spatial densities will be employed.

1.1.4 The Swedish Defence Research Agency (FOI)

This thesis is performed on behalf of the Swedish Defence Research Agency, (FOI). FOI is interested in, and carries out research relevant to space situational awareness, which the present study is a part of. These studies are carried out on behalf of mainly the Swedish Armed Forces (Försvarsmakten), but also other organizations, such as the Swedish Ministry of Foreign Affairs (Utrikesdepartementet). These are of interest to these organizations because space infrastructure is becoming a more integrated part of society, and therefore it is important to be able to determine if your access to space will worsen.

The present study is relevant to this because it helps to model and predict what may happen in a collision or explosion, and if satellites are at risk of the subsequent debris spread. It also aids in modelling the fragmentations for debris too small for ground infrastructure to detect, and may therefore give a broader risk estimate.

Chapter 2

Theory

2.1 Theoretical Background

In order to get an understanding of orbital fragmentation theory one needs to be familiar with orbital mechanics, including orbital perturbation theory. This is because the propagation of debris is not trivial, and much of the information that can be gained from studying debris is hidden behind these topics.

2.1.1 Orbital mechanics

Objects orbiting a central body follow Newton's Law of Gravitation:

$$\mathbf{F} = -G \frac{Mm}{r^2} \hat{\mathbf{r}}, \quad (2.1)$$

where M and m are the masses of the central body and the spacecraft, G is the universal gravitational constant, and \mathbf{r} is the vector between the center of mass of the central body and the spacecraft. The product GM is often denoted by μ . This equation, however, is a simplification as it does not account for disturbances such as drag, or the non-spherical gravitational effects due to the central body not being a homogeneous sphere. When observing debris, much of it is often first observed weeks after the initial event, causing the perturbations due to these disturbances to accumulate. Therefore, it is important to understand these effects to better know what impact they have on the results of the fragmentation analysis. The orbital period and the semi-major axis are concepts that will be used extensively for this purpose. The period is obtained from Kepler's Third Law:

$$P = 2\pi \sqrt{\frac{a^3}{GM}}, \quad (2.2)$$

where a is the semi-major axis, which is the average of the maximum and minimum orbital radii. These two distances are called apoapsis and periapsis, respectively.

Orbital elements

To uniquely define the position and orbit of a satellite in space, six quantities are needed [1]. Sometimes they are given in the form \mathbf{r} and \mathbf{v} , specifying the three-dimensional position and velocity relative to the origin. However, this form does not provide much information on the orbit without further calculations. Instead, the Keplerian elements are often used.

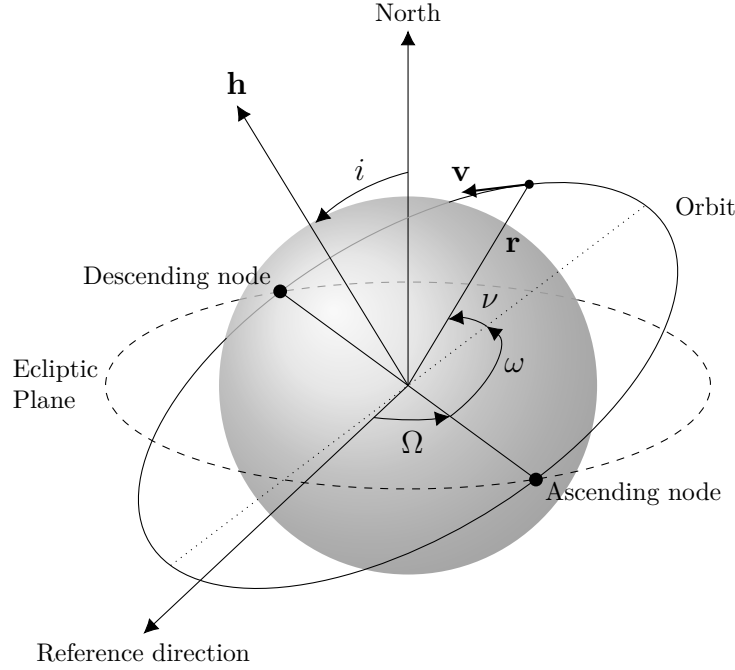


Figure 2.1: Orbital elements of an object orbiting a central body centered at the origin.

The frame used is typically chosen as an inertial frame, centered on the center of mass of a celestial body, for example an Earth-centered inertial (ECI) frame [17]. The six Keplerian elements are [18]:

- Eccentricity, e : A measure of how circular an orbit is; if an orbit has a low eccentricity it is more circular compared to orbits with higher eccentricity, which are more elliptical. If it has a value greater than or equal to one, the orbit is a parabola or hyperbola, rather than an ellipse. If the eccentricity is zero the orbit is circular.
- Semi-major axis, a : The mean of the radius of the periapsis and apoapsis.
- Inclination, i : The angle between a reference plane (often the ecliptic) and orbital plane.
- Longitude of the ascending node, Ω : Also called Right ascension of the ascending node (RAAN). It is the angle between a reference point and the ascending node. In Earth-centered frames the reference point usually points towards the first point of Aries, which is the ‘prime meridian’ of the celestial sphere.
- Argument of periapsis, ω : The angle between the ascending node to the periapsis in the orbital plane.

- True anomaly, ν : The angle between the periapsis and the orbiting object in the orbital plane.

The apoapsis, r_A , and periapsis, r_P , are called the *apsides*. Using this, we can find an expression for the semi-major axis and eccentricity:

$$a = \frac{r_A + r_P}{2}, \quad e = \frac{r_A - r_P}{r_A + r_P}. \quad (2.3)$$

Using (2.3) we can find an expression that can be used to calculate the apoapsis and periapsis using only the Keplerian elements:

$$r_A = (1 + e)a, \quad r_P = (1 - e)a. \quad (2.4)$$

Two more terms that are used are the ascending/descending *nodes*, and the ascending/descending *modes*. The nodes are illustrated in Figure 2.1, and the modes are defined as $\nu < \pi$ for the ascending mode, and $\nu > \pi$ for the descending mode. They are defined as the interval of the orbit where the radial velocity is positive or negative. Although these concepts may be difficult, they are very helpful when studying debris and fragmentations. However, perturbations will affect objects in an orbit, which is not accounted for in pure Keplerian dynamics. The two following subsections will briefly explain the main perturbations that affects debris in orbit around the Earth.

Drag

One of the concepts that affect the orbits the most, especially for objects in LEO, is aerodynamic drag. The drag force of a satellite can be expressed as [19]:

$$F_{\text{drag}} = \frac{1}{2} \rho v^2 C_D A, \quad (2.5)$$

To begin with, one can look at how drag affects circular orbits. The norm of a satellite's velocity is given by the *vis-viva equation* [18]:

$$v = \sqrt{\mu \left(\frac{2}{r} - \frac{1}{a} \right)}. \quad (2.6)$$

In a circular orbit, when $a = r$, in accordance to (2.4), the equation above simplifies to:

$$v = \sqrt{\frac{\mu}{a}}. \quad (2.7)$$

An object under the effect of drag is subject to an acceleration according to (2.5). Assuming this acceleration is the only contribution to the tangential velocity, it can also be obtained by taking the time derivative of (2.7):

$$\dot{v} = -\frac{1}{2}\sqrt{\frac{\mu}{a^3}}\dot{a} = \frac{1}{2}\rho v^2 C_D \frac{A}{m}. \quad (2.8)$$

Solving for \dot{a} , and substituting $\mu = v^2 a$, one arrives at how the drag affects the radius of the orbit [19]:

$$\dot{a} = -C_D \rho a v \frac{A}{m}. \quad (2.9)$$

Taking the time derivative of (2.2) and substituting in the equation above, one obtains [19]:

$$\dot{P} = -3\pi \frac{A}{m} C_D \rho a. \quad (2.10)$$

From these two equations one can see that both \dot{a} and \dot{P} are negative, which indicates that under the effect of drag a spacecraft will tend closer and closer to the Earth.

Although circular orbits are simple, most orbits do not fall under this category. Therefore it is important to also study elliptical orbits. For elliptical orbits, instead of doing the above analysis we instead look at the definitions of apoapsis and periapsis in (2.4). Using this equation we can see how small changes in a and e affects the heights [1]:

$$dr_{A,P} = (1 \pm e)da \pm ade, \quad (2.11)$$

where the “+” represents the apoapsis, and the “−” represents the periapsis. From intuition and (2.9) we know that the semi-major axis is expected to decrease, in other words $da < 0$. Since the atmospheric density is higher closer to the surface of the Earth we expect the drag force to be larger at periapsis compared to apoapsis. As such, the velocity decreases more at periapsis than at apoapsis, thus having a circularizing effect on the orbit. Therefore, one expects de to be negative, since a positive de would mean that the spacecraft slows down more at the apoapsis than at the periapsis, or speeds up at the periapsis. This is seen in (2.11) as both terms are negative for the apoapsis when de is negative. The equation for the periapsis in (2.11), however, has a positive second term due to the double negative, which indicates that it will decrease at a slower rate compared to the apoapsis.

Aspherical gravity

The Earth is often modeled as a perfect sphere, with *spherically symmetric* gravity. This is however not the case, since the Earth bulges out at the equator due to its spin [20]. Even though this effect is minuscule, it still has an observable effect over several orbits. One of the factors that cause this, often called the *J2 effect*, acts in the North-South direction. The derivation of this effect is shown in Appendix B, but the final result from this gives the gravitational potential of an aspherical body as a sum of the different perturbations:

$$u = -\frac{\mu}{r} \left(1 - \sum_{l=2}^{\infty} J_l \left(\frac{R_{\oplus}}{r} \right)^l P_l[\sin(\phi)] + Z(r) \right), \quad (2.12)$$

where J_l are constants, ϕ is the declination, P_l is the l th Legendre polynomial, and R_{\oplus} is the Earth's radius. The function $Z(r)$ corresponds to the *sectoral harmonics* of the central body, i.e. irregularities along the rotational axis of the central body (east-west), but is disregarded because we are focusing on irregularities along the north-south direction. In addition to this, the function $Z(r)$ is smaller in relation to the other terms and, as such, should not significantly affect the observed data during the expected time frames between fragmentation and observation [21].

In *Perturbations of satellite orbits by tesseral harmonics in the Earth's gravitational potential* ([22]), G. E. Cook shows that the semi-major and eccentricity axis varies due to the perturbation term, which is the sum term in (2.12). In particular, the effect of the oblateness on the orbiting object affects the longitude of the ascending node, Ω , and the argument of periapsis, ω , enough to need to be considered. The effect on these are (in degrees per day) [1]:

$$\frac{d\Omega}{dt} = -9.97 \left(\frac{R_{\oplus}}{a} \right)^{7/2} \frac{\cos(i)}{(1-e^2)^2}, \quad (2.13)$$

$$\frac{d\omega}{dt} = 4.98 \left(\frac{R_{\oplus}}{a} \right)^{7/2} \frac{5\cos^2(i) - 1}{(1-e^2)^2}. \quad (2.14)$$

Equation (2.13) signifies that the orbit rotates around the axis normal to the ecliptic plane, which is useful for some orbits such as Sun-synchronous orbits (SSOs). Equation (2.14) signifies *apsidal precession* of an orbit, which is when the line connecting the periapsis and apoapsis rotates about the center of mass of the central body, as seen in Figure 2.2. These perturbations are important to account for, since during the time between a fragmentation and an observation the debris may have precessed a significant bit rendering the equations used to determine different orbital parameters less accurate.

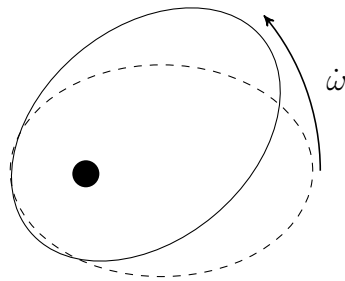


Figure 2.2: Illustration of apsidal precession of an elliptical orbit.

2.1.2 Fragmentation theory

One of the main tools in studying fragmentations in orbit is the *Gabbard diagram*. Gabbard diagrams plot the apoapsis and the periapsis of each fragment against the

respective orbital period [1]. This tool is useful as it can confirm if an explosion has occurred, estimates of the energies involved can be obtained, and risk to other satellites can be estimated. Its appearance may be very different depending on the type of orbit, and if the fragmentation happens near one of the apsides. This can be useful to determine where in the orbit a fragmentation has occurred as well.

Gabbard diagrams

From (2.2) it is clear that the period is directly related to the semi-major axis of an orbit, and therefore if the semi-major axis changes the period will change as well. The semi-major axis may change if a change in energy is introduced to the orbiting body, by for example an explosion or collision. This is shown by the equation that defines the energy of an object orbiting a central body [18]:

$$E^3 = \frac{\pi^2 \mu^2}{2P^2} \implies P^2 = \frac{\pi^2 \mu^2}{2E^3}. \quad (2.15)$$

After a breakup, each fragment will receive an energy change, often in the form of a change in velocity. The coordinate system (r, d, x) lets us define the change in orbital energy by the change in velocity in a simple manner. Here, r points radially out from the central body towards the object, d points in the downrange direction perpendicular to the surface in the direction of travel, and x completes the right-hand rule, pointing in the crossrange direction perpendicular to the velocity. The total specific energy (J/kg) after fragmentation is given by the systems kinetic and potential energy [1]:

$$E + dE = (E_k + dE_k) + (E_p + dE_p) = \frac{1}{2}[(v_d + dv_d)^2 + (v_r + dv_r)^2 + dv_x^2] - \frac{\mu}{r}, \quad (2.16)$$

where the velocity can be defined in three-dimensional space as: $v = (v_r, v_d, v_x)$. The v_x term is zero since the object has no initial velocity in the crossrange direction, by definition. dE is the change in energy due to fragmentation. Solving for this gives:

$$dE = v_d dv_d + v_r dv_r + \frac{1}{2}(dv_r^2 + dv_d^2 + dv_x^2). \quad (2.17)$$

From this equation one can directly see how perturbations in the different velocity components affect the energy and therefore the orbital period. For example, unintuitively, a change in the crossrange velocity component correlates with a small change in the orbital energy, and therefore also its period [1]. We can form a special case of (2.17) by considering near-circular orbits. In these orbits $v_d \gg v_r$, and v_x is still zero. Equation (2.17) simplifies to:

$$dE \approx v_d dv_d, \quad (2.18)$$

which signifies that a change in downrange velocity will have the greatest impact on the appearance of the Gabbard diagram. Figure 2.3 illustrates an example of a Gabbard diagram for a simulated explosion of an upper stage rocket body, in a 600 km near-circular orbit.

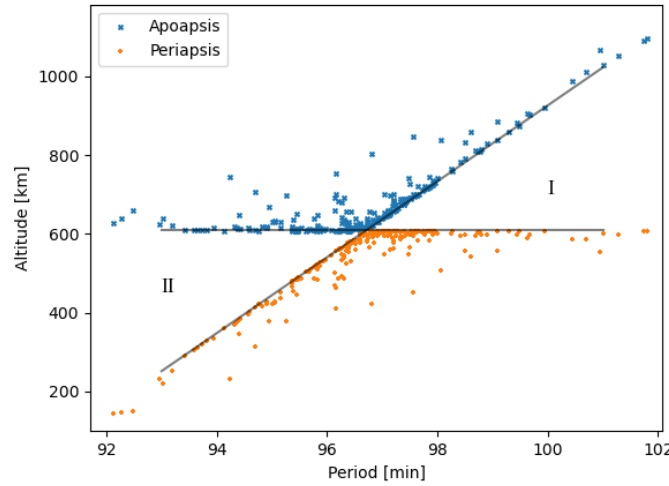


Figure 2.3: Gabbard diagram of a simulated explosion of an upper stage orbiting in a near-circular 600 km orbit.

Labeled in Figure 2.3 are two regions, I and II. These regions represent areas where fragments are usually not found and can therefore be seen as a boundary. There are two lines that make up the boundary in this near-circular special case; a horizontal and a slanted line. The horizontal line has its appearance due to the height of the explosion; the periapsis of a fragment cannot be above the original, and likewise an apoapsis cannot be below. The orbits of all fragments still need to intersect the fragmentation point, which they will not do if the periapsis is above the original periapsis, or the apoapsis is below the original periapsis.

The slanted line comes from a similar, but less intuitive, phenomena. To show why there is a slanted line we first consider the equations in (2.3). If we consider small variations, we get:

$$da = \frac{1}{2}(dr_a + dr_p). \quad (2.19)$$

Similarly, a small change in the orbital period given by (2.2) corresponds to the following:

$$dP = 3\pi\sqrt{\frac{a}{\mu}}da = \frac{3P}{2a}da. \quad (2.20)$$

We can then find an equation for the slope of the boundary lines, dr_p/dP , and dr_a/dP [1]:

$$\frac{dr_a}{dP} + \frac{dr_p}{dP} = 2\frac{da}{dP} = \frac{4a}{3P} = k. \quad (2.21)$$

For a circular orbit or an orbit where the fragmentation coincides with one of the apsides, the slope of the periapsis line is zero. The slope of the apoapsis line can then be found. The slopes of the lines for elliptical orbits can be found by considering the

true anomaly of the fragmentation. For the true anomaly, ν , being zero the object breaks up at the periapsis, and therefore we expect the periapsis to stay as an apside, since the orbits of all fragments have to intersect with the breakup point. For $\nu = \pi$ the same logic holds, except that the apoapsis line is instead horizontal. The slopes then vary between 0 and k for $\nu \in [0, \pi]$. The intersection points with the y-axis can be found by solving the equation for a line with the given slope, passing through the initial orbit.

In circular orbits the fragmentation height is trivial; simply the altitude of the orbit, however in elliptical orbits it will be more difficult to find without a Gabbard diagram. This is because in elliptical orbits the “X” shape is not always present. Instead, we see two separated clusters, as illustrated in Figure 2.4. The fragmentation altitude can be found by calculating the slopes of the fragments to get the true anomaly, which can give the altitude of the original satellite at that position. It may also be possible to backwards propagate the debris to find the altitude and time of fragmentation.

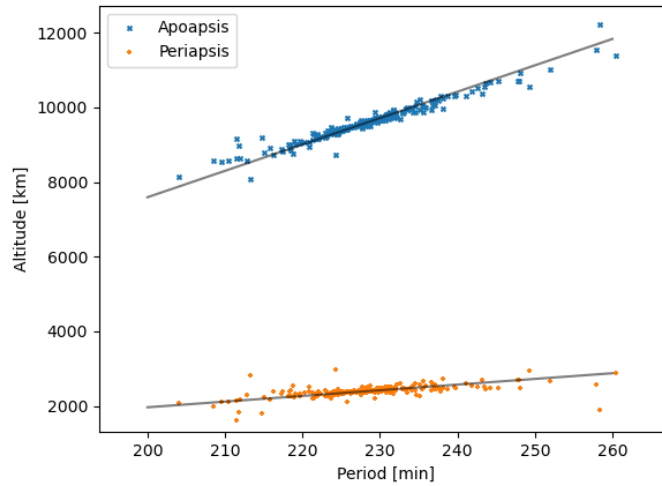


Figure 2.4: Gabbard diagram of a simulated explosion of an upper stage orbiting in an elliptical 9600 by 2400 km altitude orbit.

Figures 2.3 and 2.4 depict the Gabbard diagram directly after an explosion. This distinction is important because the energy does not always remain constant. As shown by (2.10) the period may change due to atmospheric drag, and similarly, (2.11) shows that the apoapsis and periapsis change as well. As such, due to the delay in observing the fragments, we may expect the Gabbard diagram to deviate from the instantaneous ‘ideal’ version that is depicted. Due to the apoapsis height decreasing faster than the periapsis height, this generates a “claw” shape where the points closer to the Earth, on the left side in Figure 2.3, enter region II [1]. This can be used as a rough indicator of time since fragmentation, and also as an indicator of the quality of the data.

2.1.3 Velocity perturbations of debris

Each fragment will behave differently, both due to each one having unique characteristics such as area and mass, but also because each orbit is subject to different perturbations, in particular, drag and oblateness effects. Similarly, determining the

velocity of each fragment can yield useful information regarding the fragmentation, such as cause and direction. To find the change in velocity, $d\mathbf{v}$ for each fragment, one must first consider the equations governing the debris. This is usually done with *Lagrange's planetary equations*, which include different perturbations [1]. A fragmentation event can be seen as an impulse event on each piece of debris such that $d\mathbf{v} = \mathbf{F}dt$. Using Lagrange's planetary equations, the changes in orbital parameters can be found [1]:

$$da = \frac{2}{n} \left(\frac{e \sin(\nu)}{\sqrt{1-e^2}} dv_r + \frac{a\sqrt{1-e^2}}{r} dv_d \right), \quad (2.22)$$

$$de = \frac{\sqrt{1-e^2}}{na} \left(\sin(\nu) dv_r + \left[\frac{a(1-e^2)}{er} - \frac{r}{ae} \right] dv_d \right), \quad (2.23)$$

$$di = \frac{r \cos(u)}{na^2 \sqrt{1-e^2}} dv_x, \quad (2.24)$$

$$d\Omega = \frac{r \sin(u)}{na^2 \sqrt{1-e^2} \sin(i)} dv_x, \quad (2.25)$$

$$d\nu = \frac{\sqrt{1-e^2}}{nae} \left(\cos(\nu) dv_r - \sin(\nu) \left[1 + \frac{1}{1+e \cos(\nu)} \right] dv_d \right), \quad (2.26)$$

$$d\omega = -\frac{r \cot(i) \sin(u)}{na^2 \sqrt{1-e^2}} dv_x - d\nu, \quad (2.27)$$

where the variables are the orbital elements explained in Section 2.1.1, $n = 2\pi/P$ is the mean motion, and $u = \omega + \nu$ is called the argument of latitude. Inverting these formulae to find the change in velocity can be done but has some shortcomings, for example when solving for dv_r , division by $\sin(\nu)$ is obtained, which gives an indeterminate velocity when ν is near 0 or π [1]. Instead, there is a simpler way to find the change in velocity; simply by directly comparing the measured velocities to the original velocity. The total velocity will be $\mathbf{v} = (v_r, v_d, 0)$, where v can be found using (2.6). Similarly, v_d can be found using [1]:

$$v_d = \frac{1}{r} \sqrt{\mu a(1-e^2)}. \quad (2.28)$$

This lets us find the radial velocity, v_r :

$$v_r = \pm \sqrt{v^2 - v_d^2}, \quad (2.29)$$

where the “ \pm ” corresponds to different modes of the orbits; ascending mode ($\nu < \pi$), which corresponds to “+”, and descending mode ($\nu > \pi$), which corresponds to “−”. Using the equations for energy and angular momentum, we get the perturbations:

$$dv_r = \pm \sqrt{\mu \left(\frac{2}{r} - \frac{1}{a'} \right) - \frac{\mu}{r^2} a' (1 - e'^2)} - v_r, \quad (2.30)$$

$$dv_d = \frac{\cos(\xi)}{r} \sqrt{\mu a' (1 - e'^2)} - v_d, \quad (2.31)$$

$$dv_x = \frac{\sin(\xi)}{r} \sqrt{\mu a' (1 - e'^2)}, \quad (2.32)$$

where the primed quantities represent the fragments, and the unprimed quantities represents the parameters of the original object. Again, \pm corresponds to which side of π that ν' is on. The true anomaly of the fragment is found using $\nu' = u' - \omega'$, where:

$$u' = \arcsin \left(\frac{\sin(\lambda)}{\sin(i')} \right), \quad u' = \pi - \arcsin \left(\frac{\sin(\lambda)}{\sin(i')} \right), \quad (2.33)$$

where the left equation is used for northbound trajectories, and the right equation is used otherwise. ξ is called the plane change angle, and is found via [1]:

$$\xi = \pm \arccos \frac{\cos(i) \cos(i') + \sqrt{\cos^2(\lambda) - \cos^2(i)} \sqrt{\cos^2(\lambda) - \cos^2(i')}}{\cos^2(\lambda)}, \quad (2.34)$$

where λ is the latitude of fragmentation and r is the radius of fragmentation. In this case, the “+” corresponds to $i' > i$, and the “-” corresponds to $i' < i$, in northbound trajectories. The opposite applies in southbound trajectories. Equations (2.30 – 2.32) correspond to the velocity perturbations at the time of measurement. There are many factors that may affect these perturbations between the time of measurement and time of fragmentation, especially drag and oblateness. Using (2.14) we can approximate the angle that the orbit has precessed and correct for this using:

$$\omega' = \omega'_0 - 4.98 \left(\frac{R_\oplus}{a} \right)^{7/2} \frac{5 \cos^2(i) - 1}{(1 - e^2)^2} dt, \quad (2.35)$$

where ω'_0 is the argument of perigee at observation, and dt is the time between the observation and the fragmentation.

These equations together define the change in velocity of fragments relative their parent satellite due to a fragmentation. These equations are powerful in that they can determine very specific characteristics of a fragmentation, such as the energy involved in the fragmentation, using (2.17), and even the impact angle.

2.1.4 Section summary

Another useful tool discussed is the velocity perturbations. Analysing these is especially useful when analyzing collisions due to the ability to establish a potential direction of impact. This is illustrated in Figure 2.6. The velocities are obtained by plugging in the raw orbital data Two-line element sets (TLEs) into equations (2.30) – (2.32),

and correcting for the aspherical gravity using the time and other data given in each fragment's TLE and plugging it into (2.14).

Even though the velocities are perturbed by drag, which is seen in Figure 2.5, the velocity plots still shows a clear anisotropic behaviour which cannot be explained only by (2.5). The directionality of this data indicates that there was an impact event that caused the fragmentation of the satellite, and the data even allows us to determine an approximate impact angle [12]. The velocities also allows us to perform a momentum analysis, which further may polish the impact angle, but also allows us to estimate the mass of the impactor [1]. Given that the relative velocity on impact, V , can be estimated, either directly from the data, or from simulations, and the mass of the satellite, M , is known, the mass of the impactor, m , can be obtained via conservation of momentum in the satellite's reference frame:

$$mV = (M + m)dv. \quad (2.36)$$

Similarly, using the same equation, the impact velocity can be obtained if the mass of the impactor is known instead. In this case, using the mean dv of 135.7 m/s (from Figure 2.6), the known satellite mass of 950 kg [23], and impact velocity of 8 km/s [24], the mass of the ASAT weapon is obtained as 16.4 kg. However, due to most of the impactor fragments falling back to Earth this is only an underestimation, and may be a significant one depending on the energy lost as heat, the energy required to break up the satellite, and the amount of fragments that fell back to Earth before they are observed. For reference this can be compared to the missile used by the U.S. in their ASAT test on the Solwind satellite, which had a mass of 15.9 kg [1].

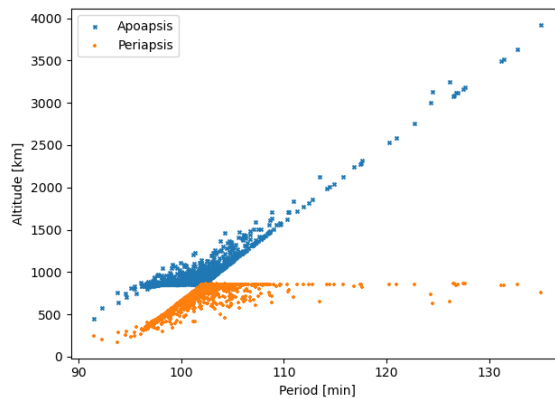


Figure 2.5: Gabbard Diagram of the fragments created by the 2007 Fengyun-1C ASAT test, with data obtained from space-track.org [16]. The ‘claw’ shape that appears due to drag can be seen on the left ‘forbidden region’, and shows that many of the fragments used in this plot were observed a long time after fragmentation [1].

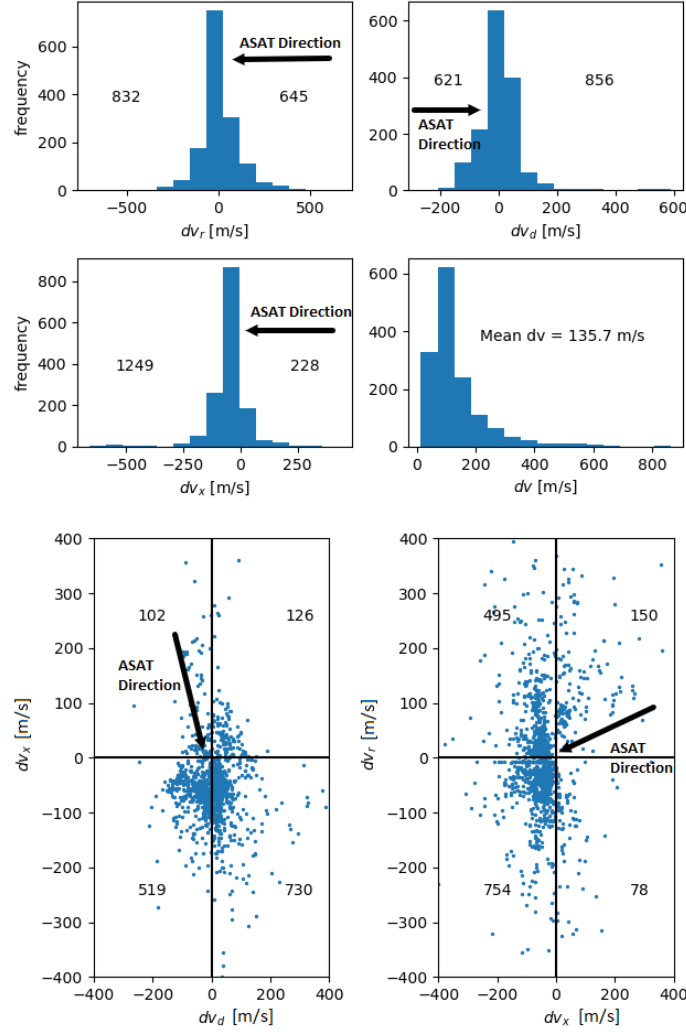


Figure 2.6: Velocity diagrams of the Fengyun-1C ASAT test showing direction of impact [12], as well as number of objects in each quadrant. Data obtained from space-track.org [16].

2.2 Risk Analysis

One of the main reasons to analyze fragmentations is to determine the impact the generated debris has on the space environment. One way to do this is to calculate the risk that debris poses to different satellites and orbits. These types of computations often require statistical tools, because of the difficulty to predict where a satellite will be, especially down to the resolutions required for these types of analyses [25]. One can compute the probability that debris will be located in a specific position, and from there generate a spatial density which can be used to calculate the flux of the distribution using [26]:

$$\text{flux} = \text{spatial density} \cdot \text{impact velocity} \equiv F = S \cdot \Delta v_i. \quad (2.37)$$

The velocity, Δv_i , is the impact velocity. The flux can be viewed as the amount of particles passing through an area per unit time during the time period that the flux is calculated for. In simpler terms, it can be assumed that a satellite moves through

a volume defined by its area and the length of a defined time interval, dt , where each particle moves at the average velocity of all objects passing through that volume. When the volume intersects the satellite, the particles that move towards the satellite will be the ones that collide with it. For instance, if the particle has the same velocity as the satellite, $\Delta v_i = 0$ m/s, and will therefore not contribute to the flux. In essence, each volume can be seen as an ‘object’ orbiting the Earth that collides with a satellite, and where the average velocity of all of the particles in the volume cancel out. So the flux will be the amount of particles in the volume intersected by the satellite multiplied by the relative velocity between the satellite and the object. This is illustrated in Figure 2.7, which can be seen as the satellite colliding with the volume at their relative velocity. If the particles move to the left, the impact velocity cannot be the satellite’s absolute velocity, since the relative velocity between them would be lower and therefore the flux would decrease compared to using the absolute velocity. This relates to the spatial density of debris as the volumes each have an average orbital velocity.

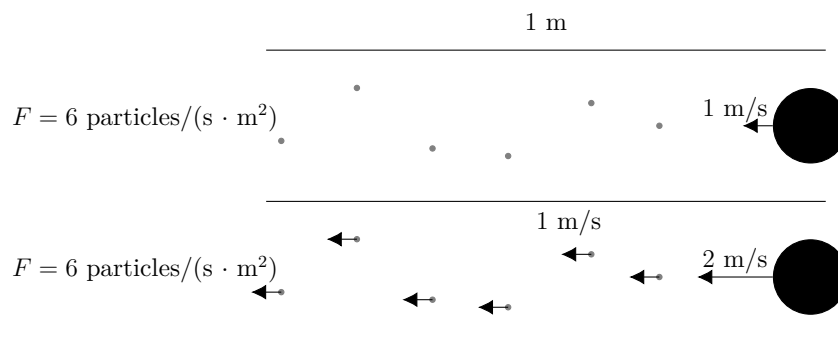


Figure 2.7: Illustration of how the relative velocity between a cloud of particles and an object effects the flux of particles through the object.

The collision risk can then be found by multiplying the flux with the area of the orbiting object and the duration that the collision risk should be calculated for, which gives the collision probability during the chosen time period. This approach is similar to the approach used to calculate collisions in kinetic gas theory. Kinetic gas theory gives us a more robust method of calculating the collision probabilities, and it can be seen that the previous approach is a special case of this [27]:

$$P_{\text{coll}} = 1 - e^{-S\Delta v_i \sigma t} \approx S\Delta v_i \sigma t, \quad (2.38)$$

where σ is the cross-sectional area of the object, and t is the time. In this report the spatial density will not be obtained by analytical approximations, but through ESA’s Meteoroid and Space Debris Terrestrial Environment Reference (MASTER) program [28], which is explained in Section 2.3.1. MASTER is used to find the spatial densities in different parts of space in order to calculate the flux and thereafter the probability. The model generated in this report can then be verified against the probabilities obtained using MASTER.

In order to obtain values for the spatial densities for varying sizes of debris, MASTER uses both data obtained from observations, as well as tests conducted on Earth to

estimate the amount of fragments for explosions and collisions, sodium-potassium (NaK) droplets from nuclear reactors, paint flakes, solid-rocket motor dust and slag, and more (see section 2.3.1). There is also the option to include meteoroid sources in the spatial density calculations. Using MASTER the Figures 2.8 and 2.9 can be obtained, showing the spatial densities of debris in Earth’s orbital environment.

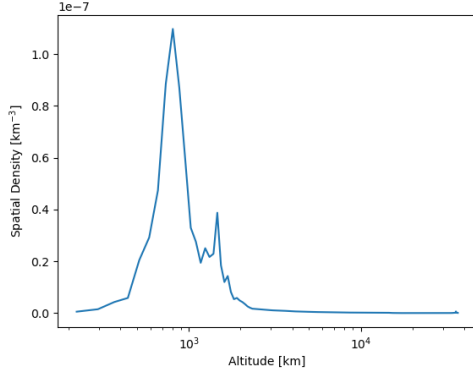


Figure 2.8: Spatial density of debris larger than 5 cm vs. altitude above Earth’s surface. The Geostationary belt can be seen to the far right as a very small peak. The horizontal axis is in log-scale. Data obtained from ESA’s MASTER for the time period 2016-11-01 [28].

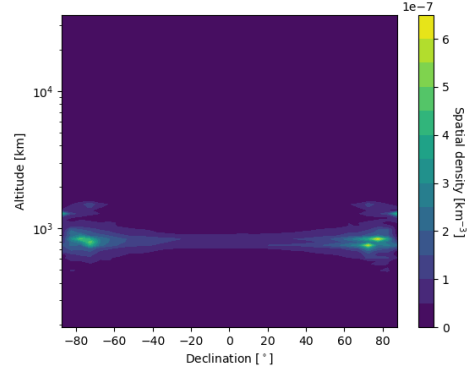


Figure 2.9: Spatial density of debris larger than 5 cm vs. altitude above Earth’s surface and declination. The SSO is clearly visible as two peaks. The vertical axis is in log-scale. Data obtained from ESA’s MASTER for the time period 2016-11-01 [28].

By propagating the orbit of an object, the flux can be calculated using the spatial density for each time step. As the area of the object is known (for example it is given in the SBM) only the impact velocity, Δv_i , is unknown in (2.38). Since there are many uncertainties, such as the eccentricity, semi-major axis, and angle of incidence of the colliding objects, the impact velocity needs to be estimated. The impact velocity frequencies can be approximated by [29]:

$$f(\Delta v_i) = (2\Delta v_i v_0 - \Delta v_i^2) \left(G \exp \left[-\left(\frac{\Delta v_i - A v_0}{B v_0} \right)^2 \right] + F \exp \left[-\left(\frac{\Delta v_i - D v_0}{E v_0} \right)^2 \right] \right) + HC(4\Delta v_i v_0 - \Delta v_i^2), \quad (2.39)$$

where $A - H$, and v_0 is given in Appendix C, equations (C.1) – (C.9). When $f(\Delta v_i)$ is negative, it is set to zero. Now this can be used to find the probability distribution function (PDF) for the impact velocity after normalizing $f(v)$ by dividing it by $\int_0^\infty f(v) dv$. This gives the probability that the impact has a specific velocity, which is demonstrated in Figure 2.10. From this the expected impact velocity between a spatial density and a satellite in a specific position can be found, given the position of the satellite.

Now all of this can be combined to assess the collision risk of an object in a general orbit. The object of interest can be propagated for the time period that one wishes to know the probability for (alternatively one can propagate for one orbital period, and extrapolate the flux to whatever time period is wanted). For each time step, dt , the flux in the volume that the object travels during that time can be obtained by [30]:

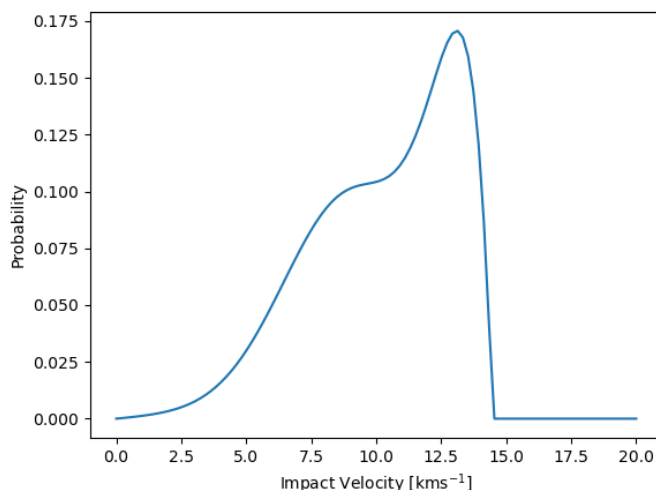


Figure 2.10: Impact velocity PDF for an object at an altitude of 400 km, with an inclination of 30° .

$$F_j = S(r_j, d_j) \Delta v_{i,j} \frac{\Delta t}{P}, \quad (2.40)$$

where d_j is the declination of the object and r_j is its altitude at time step j . The velocity $\Delta v_{i,j}$ can be obtained by generating an impact velocity using, for example, the model above. The flux is a discretization of equation (78a) in [31], namely using the average impact rate, $\dot{\eta}$:

$$\dot{\eta} = \frac{1}{P} \int_0^P \sigma \Delta v_i(\mathbf{r}) S(\mathbf{r}) dt. \quad (2.41)$$

Once the orbit is propagated, the collision probability can be obtained by using (2.38):

$$P_{\text{coll}}(T) = 1 - \exp \left(-\sigma T \sum_j F_j \right), \quad (2.42)$$

where T is the time period that one wishes to know the probability for, and σ is the average cross-sectional area of the object.

2.3 Models

The analyses required by this report necessitates the usage of several models in order to accurately simulate the dynamics and environment in space. This section is meant to explain the more important models used, and how they are used to obtain better results.

2.3.1 ESA's MASTER tool

MASTER, or Meteoroid and Space Debris Terrestrial Environment Reference, is a tool developed by ESA in order to assess the natural and man-made debris in orbit around the Earth, or one of its Lagrange points [28]. It models the debris populations based on observations, as well as models and experiments, and can project a prediction on the amount of debris in the near future as well, down to a debris diameter of 1 μm [32]. The debris included in this model are [32]:

- Explosion fragments – Using NASA's standard breakup model
- Collision fragments – Using NASA's standard breakup model
- Launch and Mission related objects
- NaK droplets – Coolant used in nuclear reactors (mainly from the Soviet RORSAT program)
- Solid rocket motor (SRM) slag – Aluminium ejected during SRM burns
- SRM dust – Smaller particles ejected during SRM burns
- Paint flakes – *Surface degradation particles* from impacts on spacecraft surfaces, oxidization, thermal cycling, and UV radiation.
- Ejecta – Debris generated when a debris particle impacts an object, cratering the surface.
- Multi-layer insulation (MLI) – Produced by fragmentation events, but behaves differently from the regular fragmentation debris.
- Meteoroids

One can specify what types of debris to include in a study, and then generate spatial densities for a given volume in space. All debris except the meteoroids are categorized as man-made. It is also possible to specify a target orbit for a given mission, and MASTER will calculate the flux encountered during this period, which can be used with (2.38) to calculate the probability of collision. MASTER will not be directly used in this report, since it does not have the capability to assess the collision probability of hundreds of fragments simultaneously, and since the density is composed of debris and not satellites. Though it will be used to validate the created model.

2.3.2 NASA's Standard Breakup Model

The NASA Standard Breakup Model (SBM) is a data-based model developed to characterize and model explosions and collisions in space. It models fragment size, area-to-mass ratio, and Δv distributions [10].

Collisions

According to the model, there are two types of collisions, *catastrophic* and *non-catastrophic* [10]. A collision is catastrophic if the impact energy is greater than 40 J/g:

$$E_I = \frac{m_1 v_i^2}{2} \cdot \frac{1}{m_2}, \quad (2.43)$$

where m_1 is the mass of the projectile or incoming satellite, m_2 is the mass of the target, and v_i is the impact velocity. If the collision is non-catastrophic, the fragmented mass is the mass of the projectile (or the smaller object) multiplied by the square of the impact velocity in km/s [33]. Likewise, if the collision is catastrophic the fragmented mass is the total mass: $m_1 + m_2$. From this, the number of fragments can be estimated, based on fitting a distribution based on observations [13]:

$$N = 0.1M^{3/4}L_c^{-1.71}, \quad (2.44)$$

where N is the number of fragments generated that are larger than a characteristic length L_c , and M is the fragmented mass. In a collision, the size of the fragments cannot be larger than any of the incoming objects, therefore the number of fragments are limited by the maximum size of the objects:

$$N = N(L_c) - N(L_{c,\max}) = 0.1M^{3/4}(L_c^{-1.71} - \underbrace{\max[L_{1,\max}, L_{2,\max}]}_{L_{c,\max}}^{-1.71}), \quad (2.45)$$

where $L_{i,\max}$ is the maximum characteristic length on object i . Equation (2.45) can then be used to generate the number of fragments created by the collision.

As an example, the collision between Iridium-33 and Cosmos-2251 was catastrophic, creating at least 600 fragments belonging to Iridium-33, and 1600 fragments belonging to Cosmos-2251 [1]. Using the masses for each satellite, 556 kg and 900 kg respectively, we can obtain the fragment counts for fragments larger than 7 cm: 1080, and 1550. The value of 7 cm is based on the minimum size that can be detected in LEO, generally being around 10 cm. Of course, the fragment counts are not exactly the same in the model and in reality, but they are relatively close to their true value. The drawback is that a different L_c can change the fragment count by hundreds of fragments as it is very sensitive; a characteristic length of 10 cm would give 587 and 842 fragments instead. Regardless, the number of fragments generated should not be seen as an exact value (nor is it true for observed data; some fragments will fall back to Earth and many remain undetected), but can be used as an approximation.

Explosions

In an explosion due to, for example, residue propellant, the dynamics are different than that of a collision, and therefore explosions have to be modeled differently in order to gain more accurate results. Based on data from the United States' Space Surveillance Network (SSN), the amount of fragments generated by an explosion follow a simple power law [13]:

$$N = 6SL_c^{-1.6}, \quad (2.46)$$

where the exponent is obtained by fitting the distribution to the gathered data and S is a unitless variable that changes depending on the type of explosion, but is often set to one [34]. For some cases, however, scaling is required, in these cases the value of S can be changed according to Table 2.1.

Table 2.1: Table containing the values of S in (2.46) for different cases [33].

Case	S
Regular rocket body	1
Proton ullage motor	0.1
Molniya orbit early warning satellite	0.25
Tsyklon third stage	0.25
Soviet ASAT	0.3
Soviet battery related explosion	0.5
EORSAT	0.6
Titan Transtage	2

Area-to-mass ratio

The second parameter generated by the SBM is the area-to-mass ratio, A/M . The equations defining A/M do not directly depend on whether the cause of fragmentation was a collision or an explosion. Instead, A/M is determined based on the characteristic length of the debris, as well as the type of object — if it is a rocket body (RB) or spacecraft (SC) the fragmentation dynamics will be different. For a rocket body the following distribution function for fragments larger than 11 cm holds [13]:

$$D_{A/M}^{RB}(\lambda_c, \chi) = \alpha^{RB}(\lambda_c) \mathcal{N}(\mu_1^{RB}(\lambda_c), \sigma_1^{RB}(\lambda_c), \chi) + [1 - \alpha^{RB}(\lambda_c)] \mathcal{N}(\mu_2^{RB}(\lambda_c), \sigma_2^{RB}(\lambda_c), \chi), \quad (2.47)$$

where:

$$\lambda_c = \log_{10}(L_c),$$

$$\chi = \log_{10}(A/M) \text{ is the variable. } A/M \text{ is obtained via: } A/M = 10^\chi,$$

$$\mathcal{N} = \text{The Normal distribution} = \mathcal{N}(\mu, \sigma, \chi) = \frac{1}{\sigma\sqrt{2\pi}} e^{-(\chi-\mu)^2/(2\sigma^2)},$$

and the rest of the variables are given in equations (D.1) – (D.5), in Appendix D. Similarly, for a spacecraft, the following equations describe the relation between the characteristic length and the area-to-mass ratio for fragments larger than 11 cm [13]:

$$D_{A/M}^{SC}(\lambda_c, \chi) = \alpha^{SC}(\lambda_c) \mathcal{N}(\mu_1^{SC}(\lambda_c), \sigma_1^{SC}(\lambda_c), \chi) + [1 - \alpha^{SC}(\lambda_c)] \mathcal{N}(\mu_2^{SC}(\lambda_c), \sigma_2^{SC}(\lambda_c), \chi), \quad (2.48)$$

where χ , \mathcal{N} , and λ_c are defined as above, and the rest of the variables are given in equations (D.6) – (D.10), in Appendix D.

For both rocket bodies and spacecraft the following distribution holds for objects smaller than 8 cm [13]:

$$D_{A/M}^{<8\text{cm}}(\lambda_c, \chi) = \mathcal{N}(\mu^{<8\text{cm}}(\lambda_c), \sigma^{<8\text{cm}}(\lambda_c), \chi), \quad (2.49)$$

where:

$$\mu^{<8\text{cm}} = \begin{cases} -0.3 & \lambda_c \leq -1.75 \\ -0.3 - 1.4(\lambda_c + 1.75) & -1.75 < \lambda_c < -1.25 \\ -1 & \lambda_c \geq -1.25 \end{cases} \quad (2.50)$$

$$\sigma^{<8\text{cm}} = \begin{cases} 0.2 & \lambda_c \leq -3.5 \\ 0.2 + 0.1333(\lambda_c + 3.5) & \lambda_c > -3.5 \end{cases} \quad (2.51)$$

For objects between 11 cm and 8 cm, a bridging function is used [13], however, a specific function, or method to find one, is not specified by the authors in the original SBM report, *Nasa's new breakup model of EVOLVE 4.0* [13], but most smooth bridging functions will yield a good transition [35]. The equations (2.47) – (2.51) were obtained by observing fragmentation events in orbit, as well as Earth based tests. The area-to-mass ratio of objects in orbit was obtained by observing their ballistic coefficient, and extracting it from there, and then the variables were fitted to the results. Particularly, the distribution for the smaller particles were obtained through a series of tests called Satellite Orbital Debris Characterization Impact Tests (SOCIT) [36].

Obtaining the values of A/M is not only useful to use in the drag equation when propagating the orbits of the fragments, but the SBM also provides a way to obtain the mass of each fragment using the relation between the characteristic length and the average cross-sectional area of the fragments [13]:

$$A_x = 0.540424L_c^2, \quad L_c < 0.00167 \text{ m}, \quad (2.52)$$

$$A_x = 0.556945L_c^{2.0047077}, \quad L_c \geq 0.00167 \text{ m}, \quad (2.53)$$

which can be used to find the mass of each fragment using $M = A_x/(A/M)$.

Fragment velocities

Once the area-to-mass ratio is obtained, each fragment can be given a characteristic velocity. Using A/M as the variable defining the velocity, the distribution for the velocity in an explosion or collision is [13]:

$$D_{\Delta v}^{\text{cause}}(\chi, \nu) = \mathcal{N}(\mu^{\text{cause}}(\chi), \sigma, \nu), \quad (2.54)$$

where ‘cause’ is the cause of fragmentation; collision (coll), or explosion (exp):

$$\chi = \log_{10}(A/M),$$

$$\nu = \log_{10}(\Delta v),$$

$$\mu^{\text{coll}} = 0.9\chi + 2.9, \tag{2.55}$$

$$\mu^{\text{exp}} = 0.2\chi + 1.85, \tag{2.56}$$

$$\sigma = 0.4. \tag{2.57}$$

Issues with the Standard Breakup Model

As may have been noticed, the equations governing the sizing of each fragment does not include a guarantee that the total mass before the fragmentation is consistent with the total mass after fragmentation, which violates the conservation of mass. Fixing this would likely require changing the number of fragments generated in the explosion.

Futhermore, velocities given are only a magnitude, but not a direction. An important aspect of analyzing fragmentations is analyzing the directions in which fragments are expelled, since this could give important clues as to what the cause was and from what direction [1].

The Standard Breakup Model also does not differentiate between which parent body the fragments belong to, which could be an important distinction for some analyses.

To fix these issues, modifications to the model has to be done. Any potential modifications implemented will be discussed in the Method chapter.

Chapter 3

Method

To accurately simulate a spacecraft fragmentation and the subsequent risk analysis it is important that the breakup model used is correctly implemented, and the risk analysis is correct. This chapter will first describe how the Standard Breakup Model is implemented, as well as how the intrinsic problems with this model can be dealt with. Then the implementation of the collision risk model is considered, and how the sub-models, such as the spatial density model, that are used can be obtained. Finally, the combination of the two models is explored to facilitate the analysis of fragmentations and the related risk analysis. A flow diagram depicting how all of the models are connected is shown in Figure 3.1.

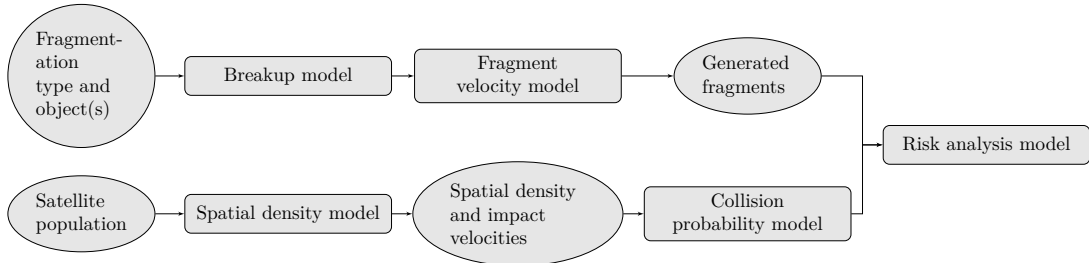


Figure 3.1: Flow diagram of how each model is used to generate a collision probability. The circles represents inputs/outputs, and the boxes represents the various models used in the process.

3.1 Breakup Model

The implementation of the Standard Breakup Model is based on the theory outlined in Section 2.3.2, with several modifications incorporated to improve it for the purpose of this thesis. As detailed earlier, the SBM suffers from several limitations, including challenges related to mass conservation and velocity direction. This section aims to explain how these limitations are tackled.

3.1.1 Mass conservation

As a stochastic model, the SBM generates values from various normal distributions, thereby creating uncertainty about the conservation of mass. This is due to the possibility of generating too few or too many fragments, or fragments with masses

that are either too high or too low. To address this, several approaches can be taken. Mass conservation could be forced, whether by changing the number of fragments, or the mass of each fragment. Both of these solutions have possible advantages and disadvantages for different applications, but in the purpose of this thesis the cumulative mass of the fragments is not a primary concern. As the focus is primarily in analyzing the distribution of fragments, with the number of fragments being a more critical factor than the total mass of all fragments when it comes to the risk analysis.

Likewise, the other approach of adjusting the mass of each fragment would require changing their areas as well, as per (2.52) and (2.53). Given that the areas are used in the calculation of collision probability, any modifications to the masses would affect the final results which is not ideal.

In summary, given that the conservation of mass is not directly relevant in this context, and that implementing this would require modifying more important variables, it has been determined that mass conservation will not be considered.

3.2 Fragment Velocity Model

The direction of each Δv resulting from a fragmentation is important as it governs the spread of the debris cloud. For instance, in the case of an ASAT test or collision, the velocity may be primarily concentrated towards the $-dv_d$ half, leading to vastly different orbits of the fragments. This is because a change in the downrange velocity has a substantial impact on the shape of the orbit itself, which can be seen in the energy equation, (2.17). Since v_d will be large in an orbit, typically much larger than v_r , a similar change in both v_d and v_r will still cause the downrange term to change the total energy more than the radial term, since $v_d dv_d > v_r dv_r$. These new orbits can have completely different risks associated with them, and as such can be useful to consider them. Since the SBM does not provide a direction for each fragment, a new model has to be implemented to account for this.

Explosion

In an explosion there may still be fragments more concentrated towards specific directions, but the total fragmentation energy will still be more evenly distributed compared to collisions. As such, the model constructed for this thesis will be built on the assumption that the spread of debris resulting from an explosion is homogeneous. Adding to this, it is impossible to predict the direction and location of an explosion. A homogeneous spherical spread of debris can be seen as an average of all possible outcomes, which will still yield useful results. In case a specific type of explosion spread is wanted this can be implemented using a similar method to the collision model, but this is outside the scope of this thesis.

To achieve a homogeneous spread, a simple method is used: for each fragment, three random numbers are generated from a uniform distribution between -1 and 1 , one for each direction. These numbers are then normalized to create a unit vector, which is multiplied by the magnitude of the change in velocity to obtain the relative velocity of the fragment. For instance, if the generated numbers are $a, b, c \in [-1, 1]$, the initial satellite's velocity is \mathbf{v} , and the total change in velocity of the fragment is dv , the

resulting velocity of the fragment \mathbf{v}' is given by:

$$\mathbf{v}' = \mathbf{v} + \frac{dv}{\sqrt{a^2 + b^2 + c^2}} \begin{bmatrix} a \\ b \\ c \end{bmatrix}. \quad (3.1)$$

The second term will generate velocity vectors uniformly spread out on a sphere. The total change in velocity can then be added to the initial velocity to get the velocity of the fragment.

Collision

There are two distinct types of collisions that are of interest: ASAT and satellite collisions. Since it is very likely that the satellites' orbits have been measured beforehand it should be possible to determine the impact angle from their respective orbits. As for ASATs, it is not as easy to predict the angle of impact, but if it can be obtained it can be used in analysis. On the other hand, if the angle is unknown, the angle of an already performed ASAT test can be obtained by finding the angle which matches the simulation results with the observed results.

To find the angle of impact of two colliding satellites, one must first propagate them to the point of impact, to find their respective velocities at this point. Assuming that the velocities are:

$$\mathbf{v}_1 = \begin{bmatrix} v_{1,x} \\ v_{1,y} \\ v_{1,z} \end{bmatrix}, \mathbf{v}_2 = \begin{bmatrix} v_{2,x} \\ v_{2,y} \\ v_{2,z} \end{bmatrix}. \quad (3.2)$$

The angle between them can be found via linear algebra. They can also be transformed from the inertial frame of reference, to the satellite's frame of reference forming unit vectors with $\hat{\mathbf{r}}$ pointing towards the satellite from the center of the Earth, $\hat{\mathbf{d}}$ will point tangential to the surface of the Earth in the direction of the velocity of the satellite, and $\hat{\mathbf{x}}$ will point in the crossrange direction, completing a right-handed system. For the radial component, one gets:

$$\hat{\mathbf{r}} = \frac{1}{\sqrt{x^2 + y^2 + z^2}} \begin{bmatrix} x \\ y \\ z \end{bmatrix}. \quad (3.3)$$

The downrange component is derived using the velocity vector. First, the radial velocity is obtained as: $v_r = \hat{\mathbf{r}} \cdot \mathbf{v}$, which can be combined with: $\mathbf{v} = \mathbf{v}_d + \mathbf{v}_r$ to find \mathbf{v}_d , using $\mathbf{v}_r = v_r \hat{\mathbf{r}}$. Then the downrange direction is found using:

$$\hat{\mathbf{d}} = \frac{1}{v_d} \mathbf{v}_d. \quad (3.4)$$

Finally, the crossrange component is found via $\hat{\mathbf{x}} = \hat{\mathbf{r}} \times \hat{\mathbf{d}}$. The impact direction in the satellite frame can then be found by converting the velocity of the second

object to this frame. The proportion of fragments that move in each direction can then be determined via conservation of momentum in the satellite's frame of reference. There are a number of ways to do this, such as Monte Carlo methods. However, since Monte Carlo methods would be time-consuming due to the large number of fragments generated, an optimization approach will be used initially to speed up the Monte Carlo process.

After setting up the equations for conservation of momentum in the chosen satellite's frame of reference, which sets its relative initial velocity to zero, an optimization problem is formulated as follows:

$$\begin{aligned} \min_{\mathbf{v}'_i} \quad & \left| -M\mathbf{v}_r + \sum_{i=1}^N m'_i \mathbf{v}'_i \right| \\ \text{s.t.} \quad & |\mathbf{v}'_i| = v'_i \\ & 1 \leq i \leq N \end{aligned} \tag{3.5}$$

This problem describes conservation of momentum before and after a collision. The total momentum of the system before the collision is $M\mathbf{v}_r$, where M is the mass of the colliding satellite, and \mathbf{v}_r is the collision velocity, both of which are known. The total momentum after collision is $\sum_{i=1}^N m'_i \mathbf{v}'_i$, which accounts for the combined momentum of each fragment, the number of fragments, N , the fragment's mass, m'_i , and the magnitude of the velocity v'_i are obtained from the SBM, but the direction, \mathbf{v}'_i , is not. Therefore, the optimization problem aims to determine the direction of each fragment's velocity such that the direction of the momentum after collision is as close as possible to the direction before collision, thereby minimizing the objective function in (3.5). The conservation relies on two assumptions; first, the direction of the momentum is conserved, second, the magnitude is not conserved. The second assumption is based on three main points: some of the collisional energy is used to break up the satellites, many of the smaller size fragments are not included, and the model is not perfect when generating the fragments (for example the mass is not conserved, as explained above). These factors makes this a viable assumption.

Solving this optimization problem can be done using a variety of approaches, but many algorithms will only find the trivial solution, where all vectors are close to parallel to \mathbf{v}_r pointing in a single direction, such that $\mathbf{v}_r \parallel \mathbf{v}'_i$. This solution is not of interest. Instead a more realistic solution can be obtained by using a stochastic process combined with a Monte Carlo process. In this process, a rotation for each fragment is randomly selected from a normal distribution centered around zero with a standard deviation, σ , which can be adjusted to control the spread of the fragments. The rotations are performed by generating three rotation angles, θ_{1-3} :

$$\theta_i \sim \mathcal{N}(0, \pi\sigma), \quad i = 1, 2, 3. \tag{3.6}$$

Following this, each vector can be rotated by multiplying it with the corresponding rotation matrices. These are obtained by plugging in the angles into $R_x(\theta_1)$, $R_y(\theta_2)$, and $R_z(\theta_3)$ below:

$$R_x(\theta_1) = \begin{bmatrix} 1 & 0 & 0 \\ 0 & \cos \theta_1 & -\sin \theta_1 \\ 0 & \sin \theta_1 & \cos \theta_1 \end{bmatrix}, R_y(\theta_2) = \begin{bmatrix} \cos \theta_2 & 0 & \sin \theta_2 \\ 0 & 1 & 0 \\ -\sin \theta_2 & 0 & \cos \theta_2 \end{bmatrix}, \quad (3.7)$$

$$R_z(\theta_3) = \begin{bmatrix} \cos \theta_3 & -\sin \theta_3 & 0 \\ \sin \theta_3 & \cos \theta_3 & 0 \\ 0 & 0 & 1 \end{bmatrix}.$$

If the conditions for conservation of direction are not fulfilled after a rotation, each velocity is reset to its initial position and the process is repeated. This is done iteratively until the resulting momentum vector has a comparable direction to the initial momentum vector. Although time-intensive, this process provides a non-trivial solution to (3.5) which accounts for random rotations imparted in the collision. However, due to the stochastic nature of generating the fragments, and the collision energies being unbounded, the sum of each fragment's momentum may be much lower or higher than the initial momentum before collision. Thus, the Monte Carlo simulation can only minimize the pointing error between the momentum vectors, and not their relative magnitudes. A comparison of solutions using the Sequential Least Squares Programming (SLSQP) algorithm in `scipy`'s `optimize` library and Monte Carlo is found in Figure 3.2. From this one can see that the global minimum found by dedicated solvers is not a very physical solution.

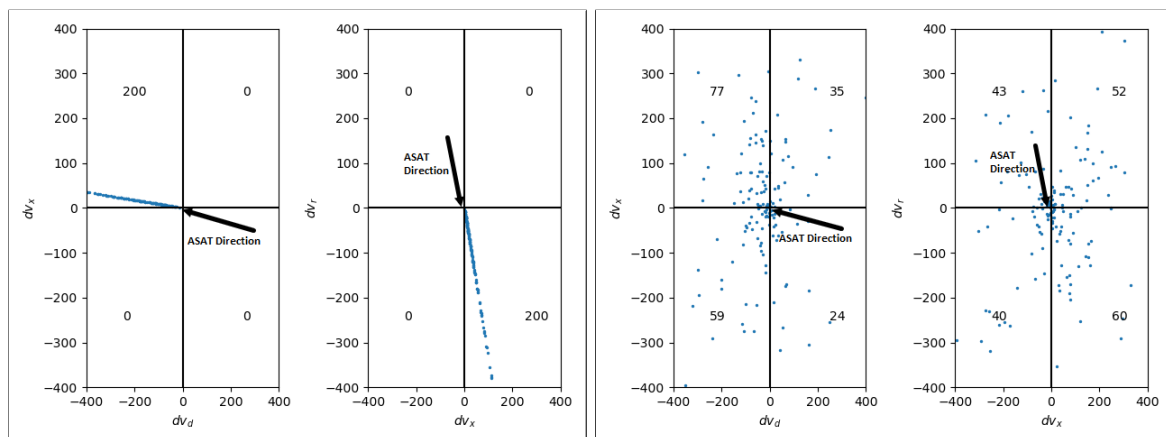


Figure 3.2: Depiction of the different possible solutions to the optimization problem. The left image is the direct solution from `scipy`'s SLSQP algorithm, whereas the right image is a solution from the Monte Carlo algorithm. Each point represents the change in velocity of a fragment.

3.2.1 Implementing the model

The foundation of the model is based on the original method outlined in Section 2.3.2, with the distinction that only fragments exceeding a length of 11 cm are considered. This choice is motivated by two main factors. Firstly, limiting the fragment size improves computation time by reducing the number of fragments generated, which would otherwise grow exponentially as the size limit decreases. Secondly, given that modern radar detection size is typically around 10 cm, restricting the analysis to fragments larger than 11 cm provides greater accuracy when comparing to real-world scenarios [16]. Additionally, this removes the need of a bridging function between the 8 to 11 cm area-to-mass ratios, as was explained in Section 2.3.2.

While most of the equations describing the characteristics of the fragments are already given in PDF form, the characteristic length of each fragment is not. Therefore, its PDF has to be generated for the characteristic lengths of each fragment. This is done using [31]:

$$p_L = \beta \frac{L_c^{-(\beta+1)}}{L_{c,\min}^{-\beta} - L_{c,\max}^{-\beta}}, \quad (3.8)$$

where β is 1.6 for explosions and 1.71 for collisions. Now, N fragments can be generated, each given an area, mass, and velocity according to (2.47) – (2.54), and a characteristic length according to the above equation. Figure 3.3 provides an overview of how the model is implemented.

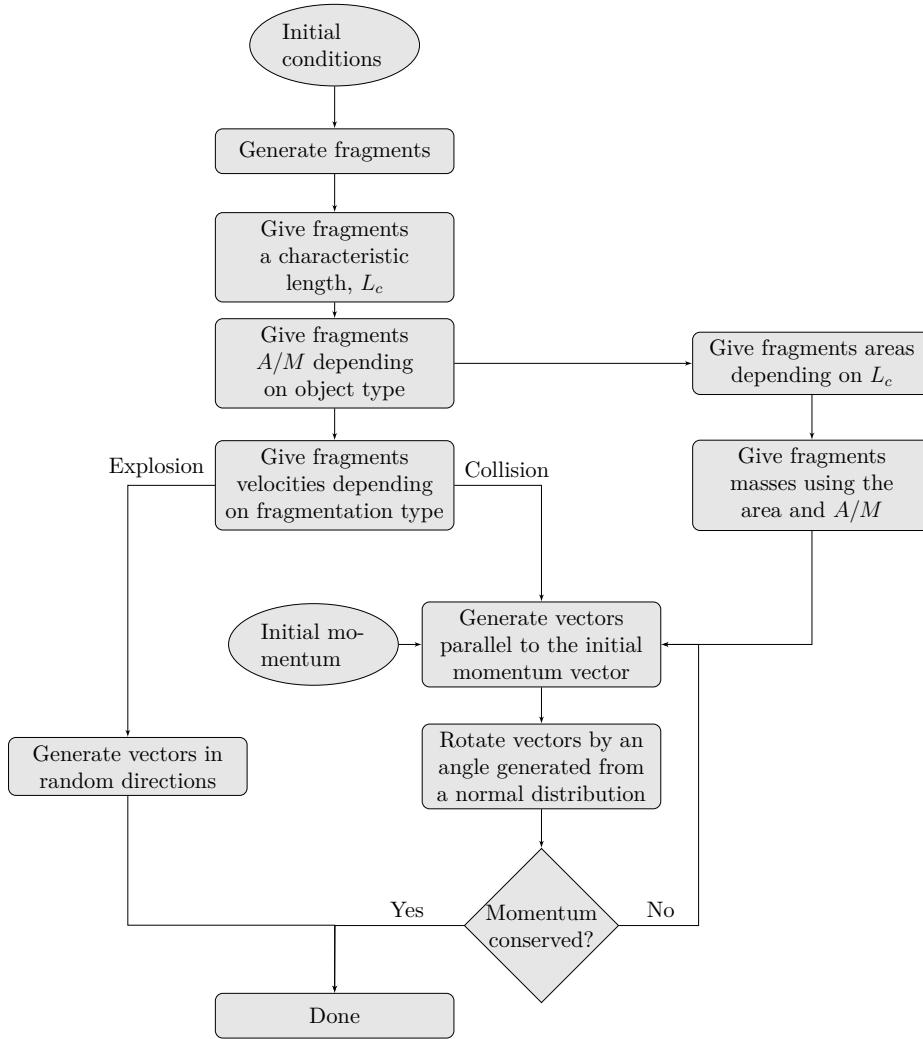


Figure 3.3: Flow diagram of the breakup model used in this thesis.

3.3 Spatial Density Model

To calculate the collision risk one needs to evaluate it with respect to a spatial density. This corresponds to calculating the collision risk relative to the satellites which are

included in the density. In this report this is done in two ways, using the spatial densities generated by MASTER, as well as spatial densities generated by propagating satellites from TLE data provided by FOI. MASTER will be used to verify the collision probability model that is generated by this report. Then, this model can be applied to any general density distribution, which in this report is the overall satellite population.

3.3.1 MASTER

The MASTER spatial density data can be obtained from the MASTER application supplied by ESA [30]. A variety of different lower limits on the sizes of debris is used, as then the model can be compared to several different cases for verification purposes. After defining the minimum debris size to consider, and the orbital domain of interest a list of spatial densities is given. The drawback of this method is that many of the built-in MASTER functions are not used when processing the data since MASTER is not directly used, and as such the algorithms using this data will differ slightly when comparing to the results from the algorithms built into MASTER.

3.3.2 TLE data

The use of TLE data when analysing the collision risk is of particular interest in cases where one desires to analyze the risk of debris colliding with satellites, as opposed to the scenario where the risk of a satellite colliding with debris, which is the focus of the MASTER algorithm. This method enables the use of any desired spatial density, which can be narrowed down to specific satellites of interest or expanded to include the entire satellite population. In this study, TLEs were obtained from FOI's internal satellite database '*El Corazon*', based on data from space-track, unless otherwise specified.

To obtain the spatial densities, the orbital domain is divided into small volumes referred to as 'bins'. For the purpose of this analysis, the longitudinal distribution perturbations are disregarded as they are not accounted for in Keplerian orbits. Therefore, it will be assumed that the longitudinal densities are uniformly distributed – which is the case for Keplerian orbits – since adding more dimensions drastically increases the computation time. Over long time periods this assumption is valid. The validity of the assumption can also be seen when it is assumed that the ascending node is uniformly distributed among the satellites [25]. We can then divide each bin into a square cross-sectioned torus, with dimensions defined by the position of each bin. An illustration of this is seen in Figure 3.4, where $d\phi = 2\pi$ is used, as the longitudinal density is assumed to be uniform.

Once all of the bins are generated, each TLE can be propagated for a full orbit, and for each time step the satellite's location is used to determine which bin it is in. This is done by locating the bin which has a center point closest to the current position of the satellite. When the bin is found the satellite's spatial density can be added to the bin. The density is calculated using the bin's volume, and the probability of the satellite being in that bin. This probability is determined by dividing the total time the satellite is in the bin by the satellite's orbital period. Then the spatial density can be calculated using:

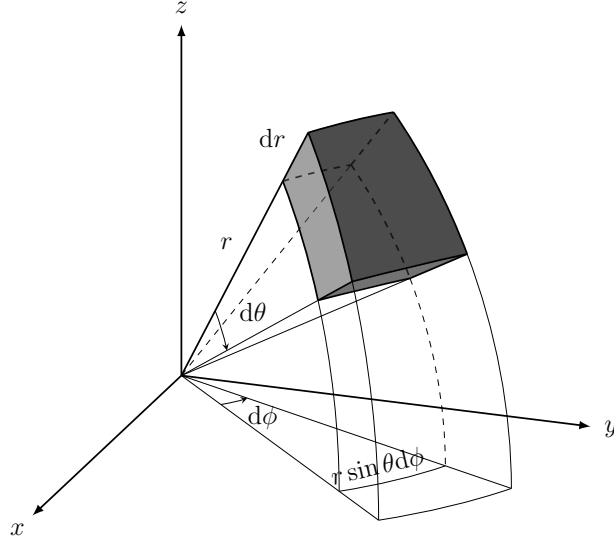


Figure 3.4: Illustration of what a bin used for calculating spatial densities looks like. For the purpose of this thesis $d\phi$ is 2π , thereby causing the differential volume to form a torus-like shape. The center of the coordinate system corresponds to the center of the Earth.

$$S_{i,j} = \frac{p_{i,j}}{V_i} = \frac{t_{i,j}}{P_j V_i}, \quad (3.9)$$

where $S_{i,j}$ is the density in bin i , with volume V_i , for satellite j , and $t_{i,j}$ is the total duration satellite j is in bin i during an orbital period P_j . After adding the spatial densities of all satellites, a total spatial density map is obtained.

3.4 Collision Probability Implementation

Equation (2.38) shows that the probability of collision is influenced by the spatial density, the impact velocity, and the area. The area is obtained from the SBM, and the spatial density is computed using the techniques described above. The impact velocity, however, is not obtained from any of these models. In this report two different ways of calculating the velocities will be proposed. The analytical approximation of the impact velocity described in [29] and shown in (2.39), and a data-driven approach based on the average velocity computed for each of bin, as discussed in the previous section, will be used.

The analytical approximation of the impact velocity was originally only intended for use in the LEO domain. Although most of the operational satellites operate in LEO, which renders (2.39) accurate for these regions, it is not as accurate further from Earth. While all equations in Appendix C help determine the impact velocity, (C.9) includes a term for the circular velocity at around an altitude 400 km. In this report, a modification to (C.9) is proposed in an attempt to generalize the distribution beyond LEO by modifying it to the following formula:

$$v_0 = \begin{cases} \sqrt{\frac{\mu}{r}}/1000 - 0.45 + 0.015(i - 30^\circ) & i < 60^\circ \\ \sqrt{\frac{\mu}{r}}/1000 & i \geq 60^\circ \end{cases}. \quad (3.10)$$

Now the impact velocity will be more generalized, but this modification has not been validated to be as accurate for higher orbits as for low orbits. This will be done by comparing it with the results obtained from MASTER. The reason for including this is that it makes it easier to build on the model in the future if one wants to extend to an analytical or semi-analytical model, for example an expansion on the SBM. If this modification proves to be unusable, the other method can be employed instead.

Once a model for the impact velocity is obtained the total flux can be calculated. The flux for a given satellite is found by propagating the satellite and adding the local flux at each time step, using (2.37). Each relevant parameter can be acquired using the models explained in the previous sections. Since the spatial densities are discrete, a rectangular bivariate spline interpolation is used to make the distribution continuous, which is applied together with the propagation to find the densities for a wider range of positions. The total flux is obtained by adding the local fluxes using (2.40):

$$F_{\text{tot}} = \sum_i F_i = \sum_i \frac{S(\mathbf{r}_i)v(\mathbf{r}_i)}{P} \Delta t, \quad (3.11)$$

where $S(\mathbf{r}_i)$ is the interpolated density, $v(\mathbf{r}_i)$ is the impact velocity, Δt is the time step of the propagation, and P is the orbital period. Finally, the collision probability is obtained by using this flux in (2.42).

3.5 Model Verification

When a model is generated it can be verified whether it is accurate by comparing it to real world scenarios, such as real collisions and, explosions. The collision probability can be verified by comparing it against the probability generated by the MASTER model. Once both aspects of the model have been verified, they can be combined to create a model capable of analyzing fragmentations and the risk accompanying them.

3.5.1 Verifying the breakup model

The collision model is validated by simulating the collision of the Iridium-33 and the Cosmos-2251 satellites, and comparing the Gabbard diagrams which have been generated with the Gabbard diagrams of observed data. Potential tuning of the simulation parameters (such as how accurate the momentum direction needs to be, and fragment rotation angles) is done to ensure accurate results. Similarly, the explosion model is compared to two cases; a rocket body and a spacecraft explosion. These cases are simulated and compared to previous real-world events to verify each model. Again, tuning of the parameters can potentially be done to improve the model. The validation is done by comparing the model to the explosion of the Delta upper stage that launched NOAA-3 satellite, as well as the explosion of the NOAA-16 satellite.

To analyse the fragments using the theory explained in Section 2.1.3, the location of the fragmentations, as well as the orbital parameters of the parent body has to be known. The Iridium-33 – Cosmos-2251 collision occurred on the 10th of February 2010, 776 km above Russia at 72.51°N, 97.88°E, the Delta upper stage that carried NOAA-3 exploded on the 28th of December, 1973, 1515 km above the Pacific Ocean, at 37°S, 181°E [1],

and NOAA-16 exploded on the 25th of November, 2015, 855 km above the Barents Sea at 77.5°N, 48.8°E [23]. Using this, together with the values presented in Table 3.1, the theory explained in Section 2.1.3 can be applied to the fragments.

Table 3.1: Orbital parameters of the Iridium-33 and Cosmos-2251 satellites, prior to collision, as well as the NOAA-3 Delta upper stage, and the NOAA-16 satellite prior to explosion [23].

Parameter	Iridium-33	Cosmos-2251	Delta RB	NOAA-16
e	0.0002251	0.0016015	0.00057	0.00113
a (km)	7155	7164	7885	7226
i (°)	86.34	74.04	102.4	98.92
P (min)	100.4	100.6	116.4	101.9
m_{dry} (kg)	556	900	840	1475

3.5.2 Verifying the collision probability model

The collision probability model is verified by propagating different types of orbits for different spatial densities generated by MASTER, calculating the total flux and finally calculating the probability. This can then be compared to the probability given by MASTER by considering the total flux that it generates. To generate a flux in MASTER the following steps needs to be followed:

1. Specify the orbit of interest.
2. Generate data for the cumulative flux.
3. In the generated data file, find the flux of debris with the size of interest.
4. Plug the flux, area, and time of interest into (2.38) to find the collision probability.

Because MASTER uses a slightly different method to convert from the density domain to the flux domain it is expected that the results are not going to be the same. The verification is done to see if the difference between the methods are adequately small. Different sizes of debris, as well as different types of orbits will also be compared to make sure that the models are similar in as many aspects as possible. Debris ranges >1 , >5 , and >10 cm will be used. If all of these tests give similar results to the results obtained from MASTER, then one can verify that the models are similar and that it can be generalized for other spatial densities as well.

Different orbits are chosen to measure the flux in different domains, as such both circular, eccentric and inclined orbits are used to find the flux. The orbits chosen are shown in Table 3.2, in the same format they would be input into MASTER to find the flux.

Table 3.2: Parameters used when verifying the flux model.

Orbit #	a (km)	e	i (°)	ω (°)
1	7136	0.001	98.6	200.0
2	30000	0.7	14.2	0.0
3	8000	0.1	0.0	50.0
4	15000	0.4	90.0	10.0

Chapter 4

Results

This chapter presents results and minor analysis of the breakup model by comparing the fragmentation of various real-world cases, including a Delta upper stage explosion, the NOAA-16 spacecraft explosion, and the Iridium–Cosmos collision. A comparison provides information to confirm that the model behaves as expected and produces accurate results. Similarly, results from the spatial density and risk model are presented and compared as well.

4.1 Breakup Model Results

The breakup model is verified by comparing fragmentations for various real world cases. The following section will provide these comparisons, as well as relevant numbers that are used to obtain these results.

4.1.1 Validation

To verify the breakup model, it will be compared to three different real world cases to make sure that it behaves as expected. These three cases are: a Delta upper stage explosion (rocket body explosion), the NOAA-16 explosion (spacecraft explosion), and the Iridium–Cosmos collision. These cases are chosen because they cover the main parts of the breakup model, they are spread out over time and therefore include both recent and older materials and technologies, as well as they are well documented.

Explosion

The true anomaly of the Delta 1 upper stage at the time of fragmentation, $\nu = 192^\circ$, indicates that it was in ascending mode at the time of fragmentation, which determines the sign of (2.29). Using this, the sign of the radial velocity is defined and the initial velocities of the object are:

$$v_d = \frac{1}{r} \sqrt{\mu a (1 - e^2)} = 7.11 \text{ km/s}, \quad (4.1)$$

$$v_r = \frac{1}{r} \sqrt{\mu a e^2 - \frac{\mu}{a} (r - a)^2} = 2.18 \text{ m/s}. \quad (4.2)$$

Using FOI's database the TLEs of the fragments can be found, and using the theory described in Section 2.1.3 the debris can be processed. This yields Figures 4.1 – 4.3.

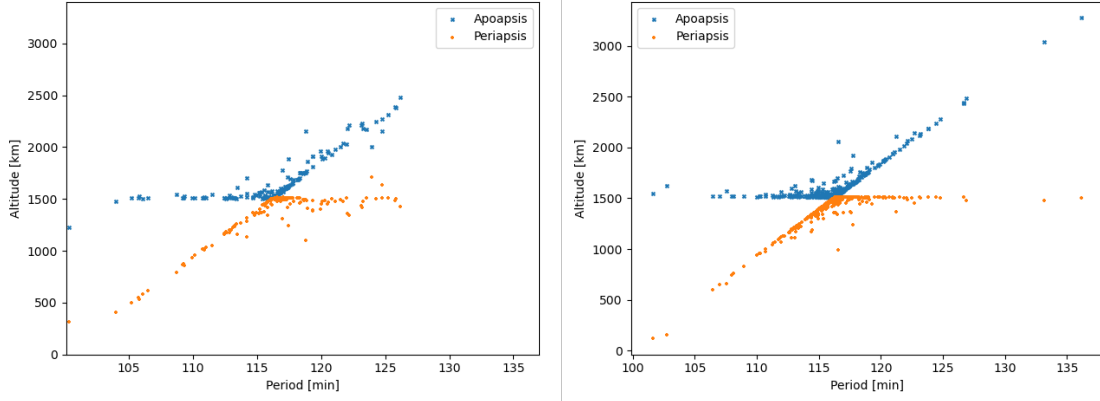


Figure 4.1: Gabbard diagram of the NOAA-3 Delta 1 upper stage explosion (left), as well as the simulated Gabbard diagram from the model (right).

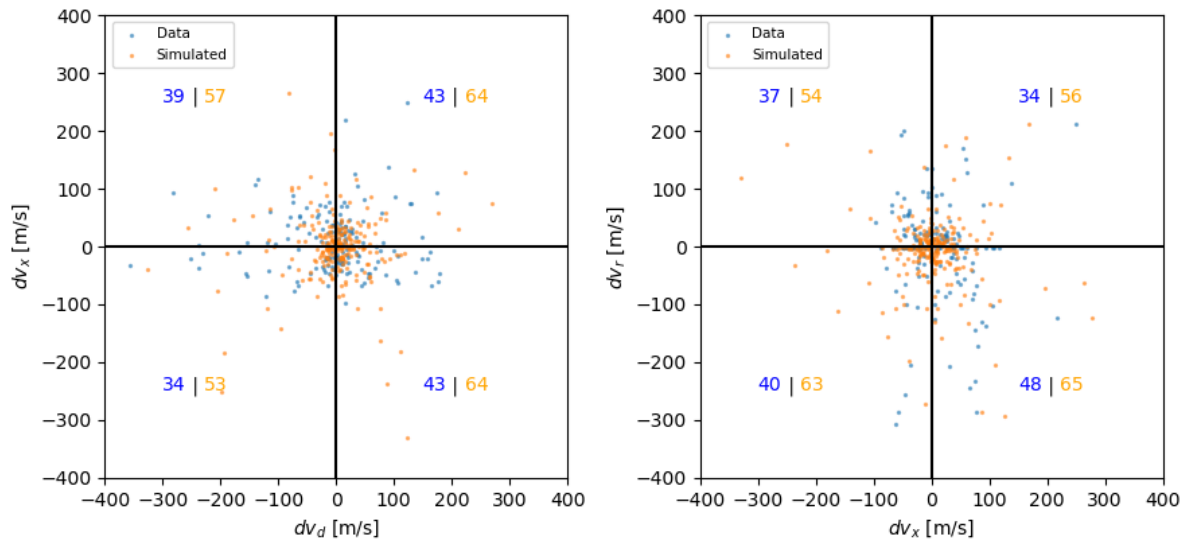


Figure 4.2: Velocity perturbations of the NOAA-3 Delta 1 upper stage explosion (blue), as well as the simulated results from the model (orange). The numbers indicate the number of fragments on each octant, on the format: Data | Simulated.

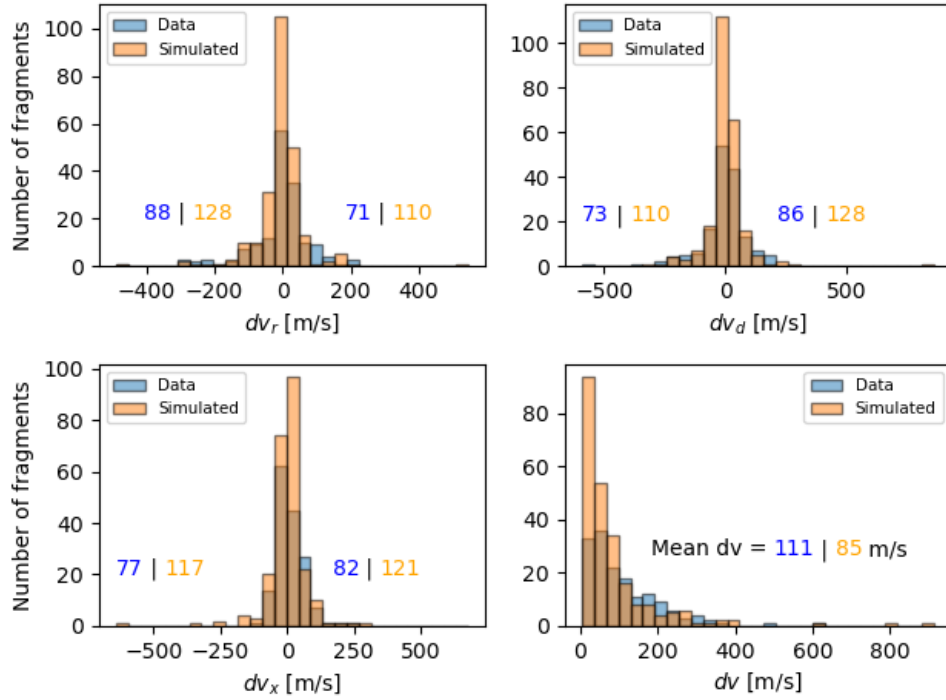


Figure 4.3: Velocity perturbation histograms of the NOAA-3 Delta 1 upper stage explosion (blue), as well as the simulated results from the model (orange). The numbers indicate the number of fragments on each half, on the format: Data | Simulated.

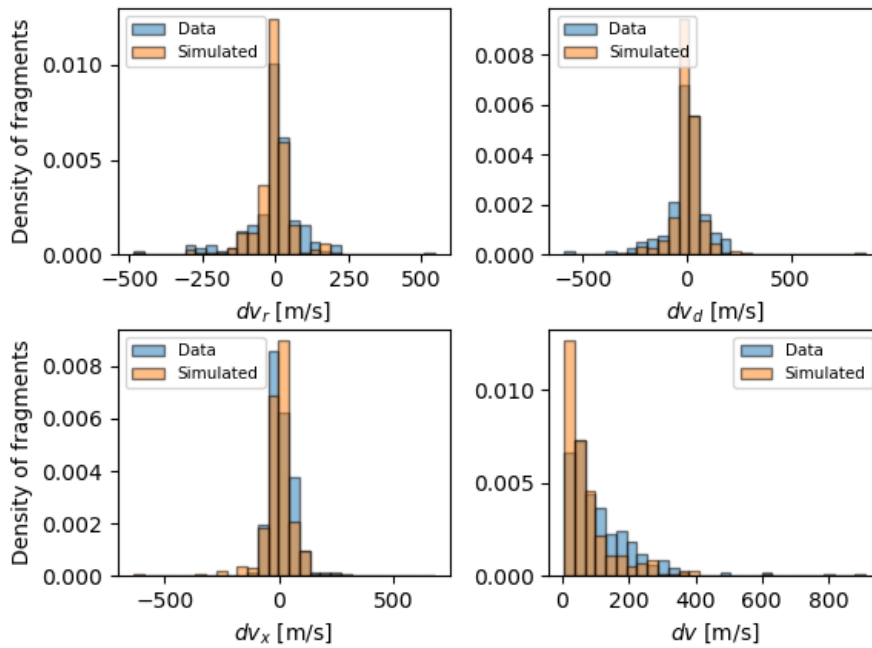


Figure 4.4: Normalized velocity perturbation histograms of the NOAA-3 Delta 1 upper stage explosion (blue), as well as the simulated results from the model (orange). The numbers indicate the number of fragments on each half, on the format: Data | Simulated.

From Figures 4.1 – 4.4 it can be seen that the simulated explosion has a similar distribution as the observed data. The most obvious difference is the number of fragments, which can be changed in the SBM by changing the characteristic length. The number of fragments of the observed data is based on when the fragments were observed, as well as the resolution of the radar equipment used. Using a minimum characteristic length, $L_{c,\min} = 0.11$ m, the number of objects obtained from the SBM is 238 fragments, compared to the number of fragments used in the data, which is 159 fragments. However, 197 fragments have been observed since the fragmentation [1]. The reason fewer fragments are used than the total amount of observed fragments is because some of the fragments are observed too late, when perturbations may have had more impact on the orbits.

Similarly, for the NOAA-16 explosion, the true anomaly, 313° , found by propagating the original satellite to the point of fragmentation from its latest available TLE before fragmentation, indicates that the object was in descending mode at the time of fragmentation. Now the initial velocities of the object are found:

$$v_d = 7.42 \text{ km/s}, \quad (4.3)$$

$$v_r = -5.37 \text{ m/s}. \quad (4.4)$$

described in Section 2.1.3 the debris can be processed. This gives Figures 4.5 – 4.7.

Using FOI's database the TLEs of the fragments can be found, and using the theory

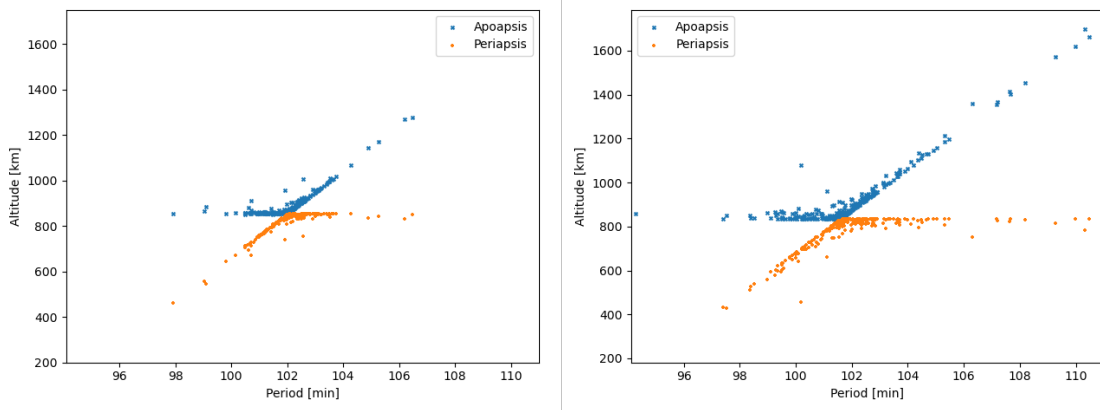


Figure 4.5: Gabbard diagram of the NOAA-16 explosion (left), as well as the simulated Gabbard diagram from the model (right).

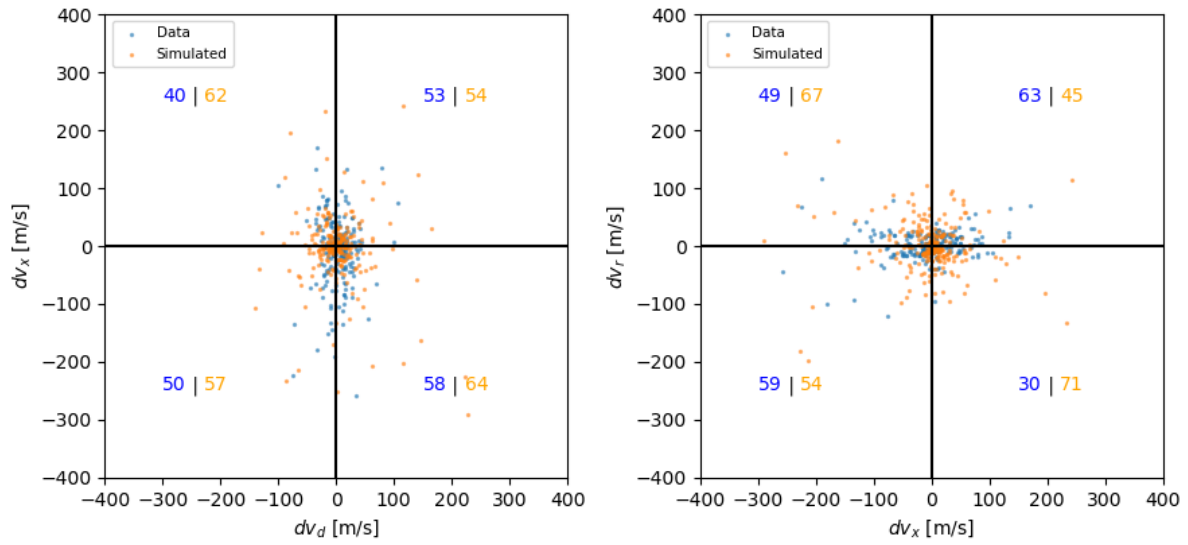


Figure 4.6: Velocity perturbations of the NOAA-16 explosion (blue), as well as the simulated results from the model (orange). The numbers indicate the number of fragments on each octant, on the format: Data | Simulated.

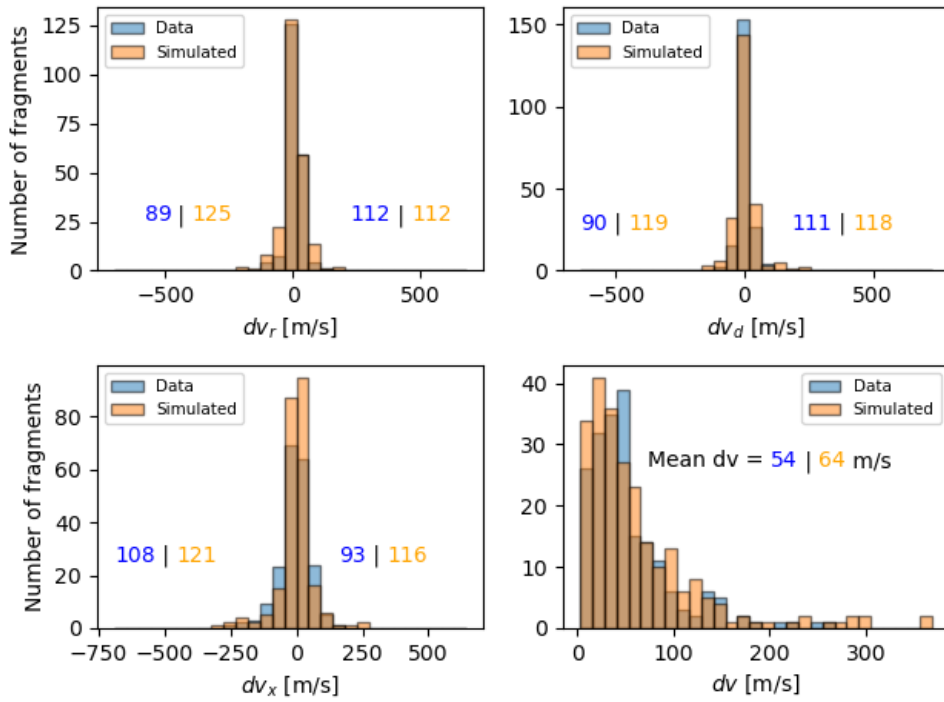


Figure 4.7: Velocity perturbation histograms of the NOAA-16 explosion (blue), as well as the simulated results from the model (orange). The numbers indicate the number of fragments on each half, on the format: Data | Simulated.

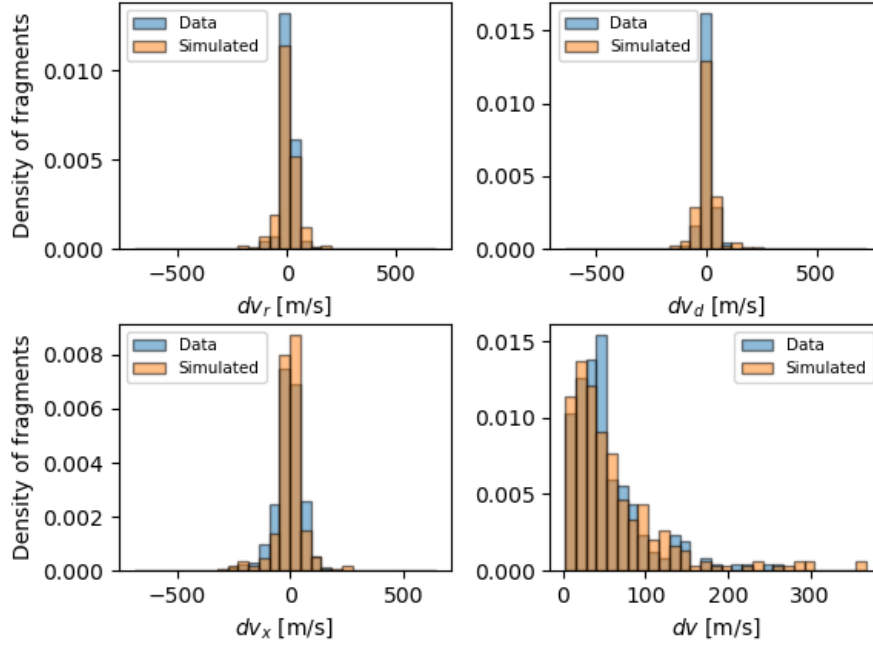


Figure 4.8: Normalized velocity perturbation histograms of the NOAA-16 explosion (blue), as well as the simulated results from the model (orange). The numbers indicate the number of fragments on each half, on the format: Data | Simulated.

From Figures 4.5 – 4.8 it can be seen that the simulated explosion has a similar distribution as the observed data. Using a minimum characteristic length, $L_{c,\min} = 0.11$ m, the number of objects obtained from the SBM is 236 fragments, compared to the number of observed fragments used in the computations, which is 201. However, at least 287 fragments have been observed since the fragmentation [1].

Collision

A similar analysis done for the collision between the Iridium-33 and Cosmos-2251 satellites yields the following results. The true anomalies found through propagation are, $\nu_{\text{Iridium-33}} = 243^\circ$, and $\nu_{\text{Cosmos-2251}} = 13^\circ$, which indicates that the satellites were in descending and ascending mode respectively at the time of fragmentation. However, other studies have been made based on TLE data, as well as other radar observations, which places the Cosmos-2251 satellite in descending mode. It is important to note that it can be difficult to accurately determine the true anomaly for some cases, especially when they are in near-circular orbits as they are in this case [1]. As such both ascending and descending modes will be used for the Cosmos-2251 satellite. The initial velocities of the satellites can be found:

$$\begin{array}{ll} \text{Iridium-33} & \text{Cosmos-2251} \\ v_d = 7.5 \text{ km/s,} & v_d = 7.5 \text{ km/s,} \end{array} \quad (4.5)$$

$$v_r = -5 \text{ m/s,} \quad v_r = \pm 2 \text{ m/s.} \quad (4.6)$$

Using FOI's database, the TLEs of the fragments can be found, and using the theory described in Section 2.1.3 the debris can be processed to give the Gabbard diagrams below. Through testing, it is found that the value of the standard deviation of the angle each fragment's velocity is rotated by, $\pi\sigma$, defined in (3.6), to give an accurate distribution similar to the real-world observation, within a reasonable amount of time, is $\pi\sigma = 0.32$.

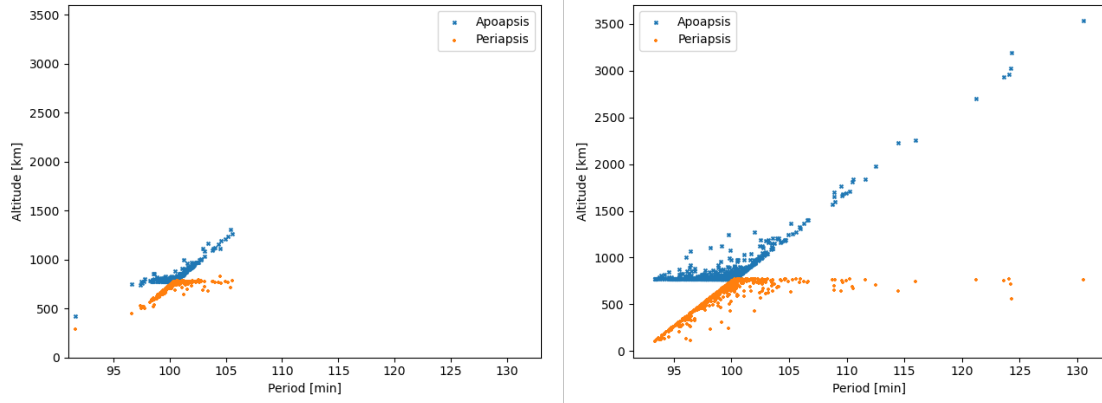


Figure 4.9: Plots showing the Gabbard diagram of Iridium-33 (left), as well as the simulated results from the model (right).

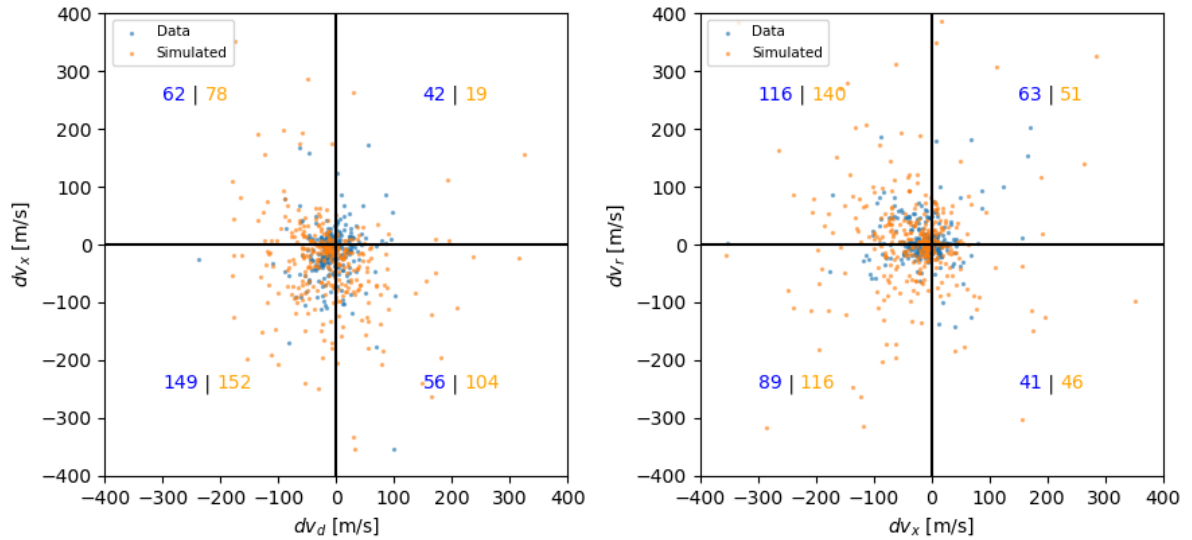


Figure 4.10: Velocity perturbations of Iridium-33 (blue), as well as the simulated results from the model (orange). The numbers indicate the number of fragments on each octant, on the format: Data | Simulated.

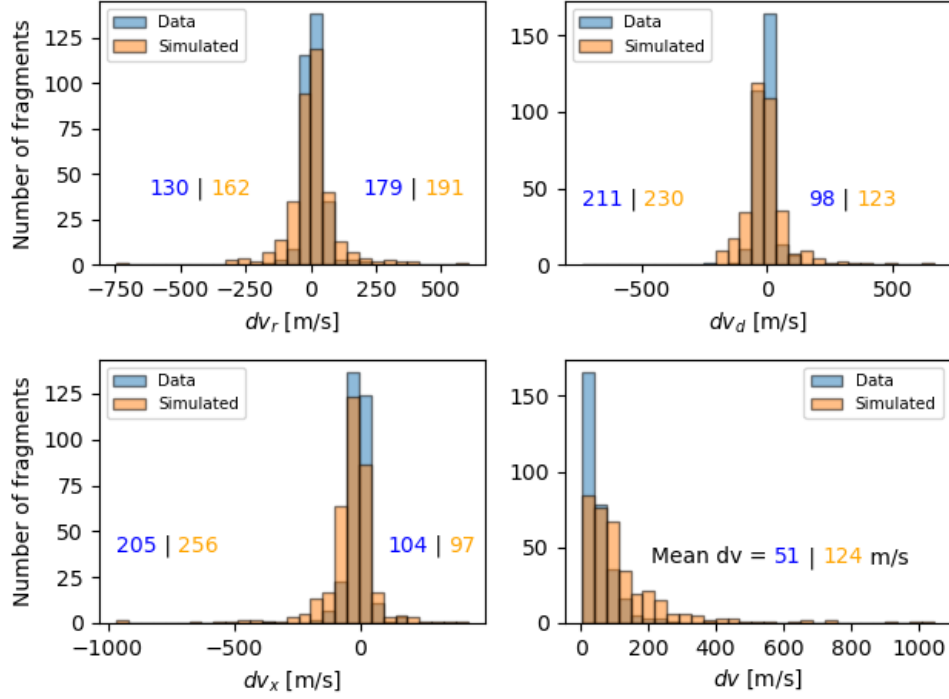


Figure 4.11: Velocity perturbation histograms of Iridium-33 (blue), as well as the simulated results from the model (orange). The numbers indicate the number of fragments on each half, on the format: Data | Simulated.

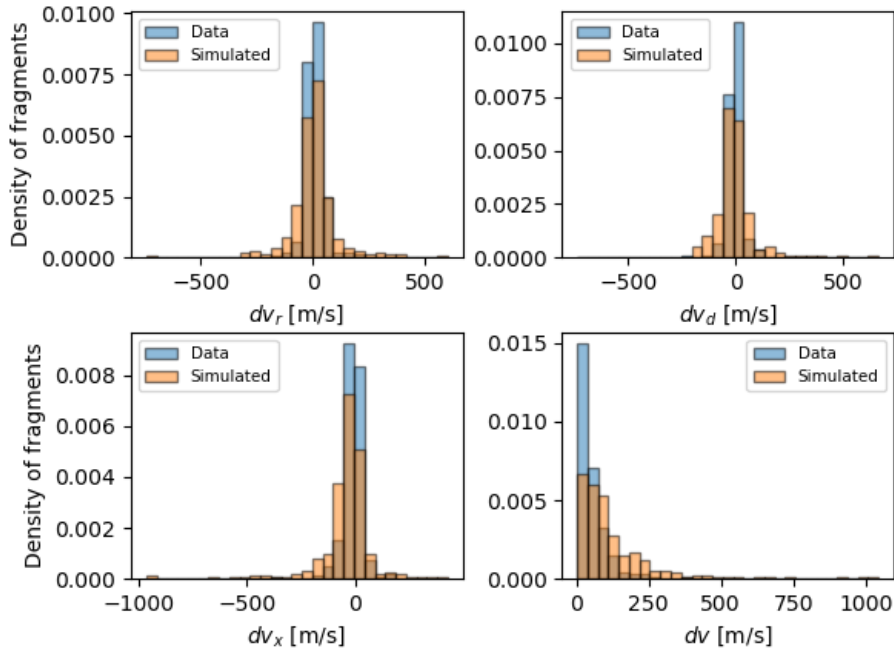


Figure 4.12: Normalized velocity perturbation histograms of Iridium-33 (blue), as well as the simulated results from the model (orange). The numbers indicate the number of fragments on each half, on the format: Data | Simulated.

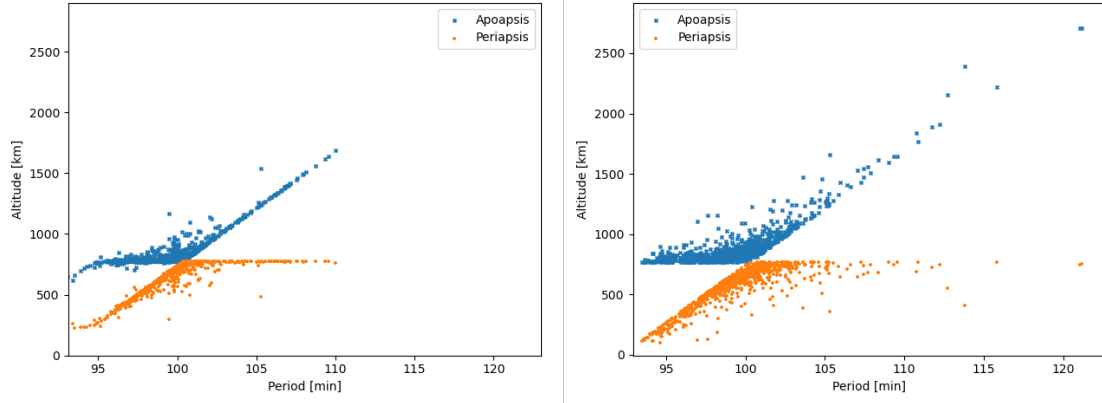


Figure 4.13: Gabbard diagram of Cosmos-2251 (left), as well as the simulated Gabbard diagram from the model (right).

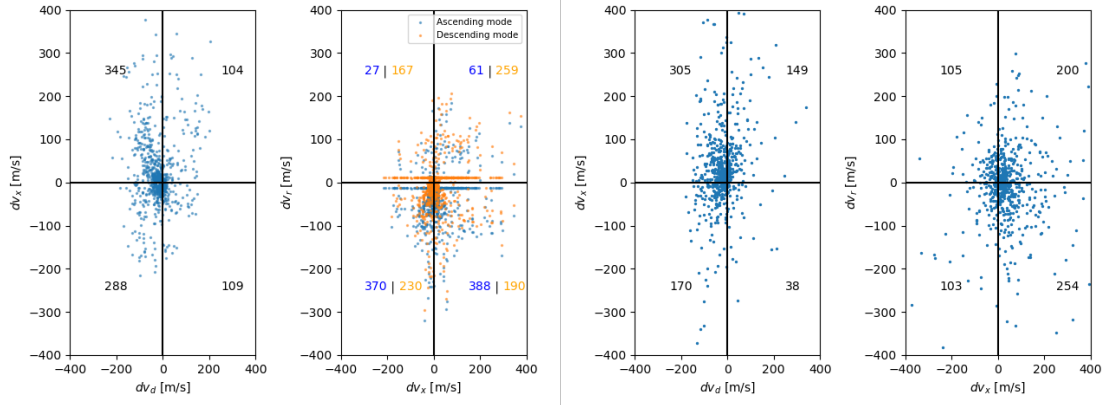


Figure 4.14: Velocity perturbations of Cosmos-2251 for both ascending and descending modes. The number of fragments in each quadrant is also specified in the format ascending | descending (left). The simulated results from the model are also shown (right).

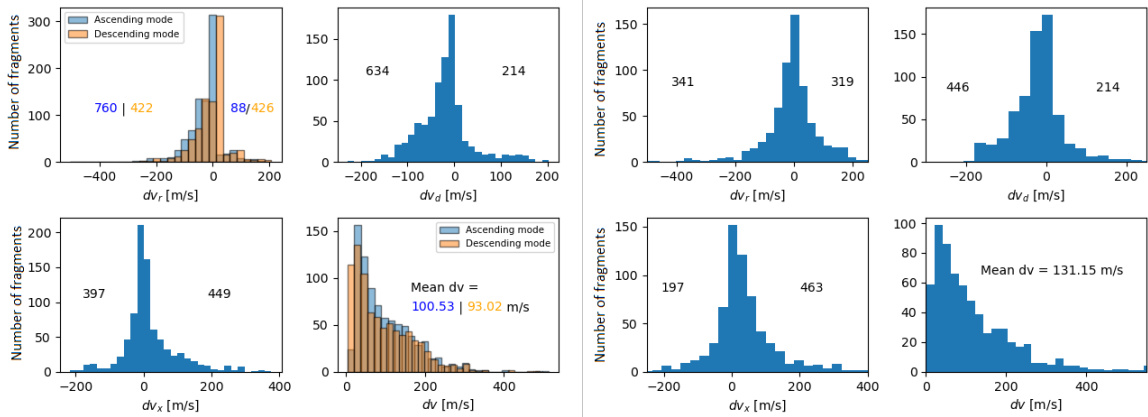


Figure 4.15: Velocity perturbation histograms of Cosmos-2251 (left), as well as the simulated results from the model (right).

These results demonstrates that the implemented model can get similar distribution of fragments for each quadrant compared to observed data. The number of fragments

generated, 305 for the Iridium-33 satellite, and 631 for the Cosmos-2251 satellite, significantly differ from their real-life counterparts, but in general the Cosmos-2251 fragments characteristics are more accurate. The horizontal lines in the Cosmos-2251 scatter plot appear due to much of the data from the Cosmos-2251 fragments are significantly affected by drag. As such (2.30) does not have real solution, and by convention dv_r is then set to $-v_r$ [1].

4.2 Spatial Density Model Results

The spatial density model is verified by generating a flux using the spatial densities obtained from MASTER and comparing it to the flux values generated by MASTER's built-in algorithms. The raw spatial densities of man-made objects larger than 1, 5, and 10 cm (obtained from MASTER) is used, and can be seen in Figure 2.9. This gives the results displayed in Table 4.1.

Table 4.1: Flux [$\text{m}^{-2} \text{y}^{-1}$] for the orbits specified in Table 3.2, using a spatial density containing debris larger than 1, 5, and 10 cm, using the analytical and simulated impact velocity model. The ratio between the model values and the MASTER value is also provided to facilitate comparisons.

Orbit # > 1 cm	Model flux (analytical)	Model flux (simulated)	MASTER flux	Ratio (analytical)	Ratio (simulated)
1	$0.4749 \cdot 10^{-3}$	$0.2515 \cdot 10^{-3}$	$0.3330 \cdot 10^{-3}$	1.43	0.75
2	$0.1140 \cdot 10^{-5}$	$0.7690 \cdot 10^{-6}$	$0.3221 \cdot 10^{-6}$	3.54	2.39
3	$0.6167 \cdot 10^{-4}$	$0.5112 \cdot 10^{-4}$	$0.5933 \cdot 10^{-4}$	1.04	0.86
4	$0.1747 \cdot 10^{-5}$	$0.1101 \cdot 10^{-5}$	$0.1289 \cdot 10^{-5}$	1.36	0.85
> 5 cm					
1	$0.6390 \cdot 10^{-4}$	$0.3461 \cdot 10^{-4}$	$0.4693 \cdot 10^{-4}$	1.36	0.74
2	$0.9417 \cdot 10^{-7}$	$0.5768 \cdot 10^{-7}$	$0.1968 \cdot 10^{-7}$	4.78	2.93
3	$0.6001 \cdot 10^{-5}$	$0.5084 \cdot 10^{-5}$	$0.5673 \cdot 10^{-5}$	1.06	0.90
4	$0.1041 \cdot 10^{-6}$	$0.6497 \cdot 10^{-7}$	$0.7994 \cdot 10^{-7}$	1.30	0.81
> 10 cm					
1	$0.3226 \cdot 10^{-4}$	$0.1731 \cdot 10^{-4}$	$0.2393 \cdot 10^{-4}$	1.35	0.72
2	$0.4868 \cdot 10^{-7}$	$0.2847 \cdot 10^{-7}$	$0.7819 \cdot 10^{-8}$	6.23	3.64
3	$0.3106 \cdot 10^{-5}$	$0.2662 \cdot 10^{-5}$	$0.2967 \cdot 10^{-5}$	1.05	0.90
4	$0.4022 \cdot 10^{-7}$	$0.2519 \cdot 10^{-7}$	$0.3100 \cdot 10^{-7}$	1.30	0.81

The spatial density of the satellites in orbit around the Earth can now be found using the theory in Section 3.3.2. Using a radial bin size of 21 km, and a declination size of 2.5° one obtains Figure 4.16.

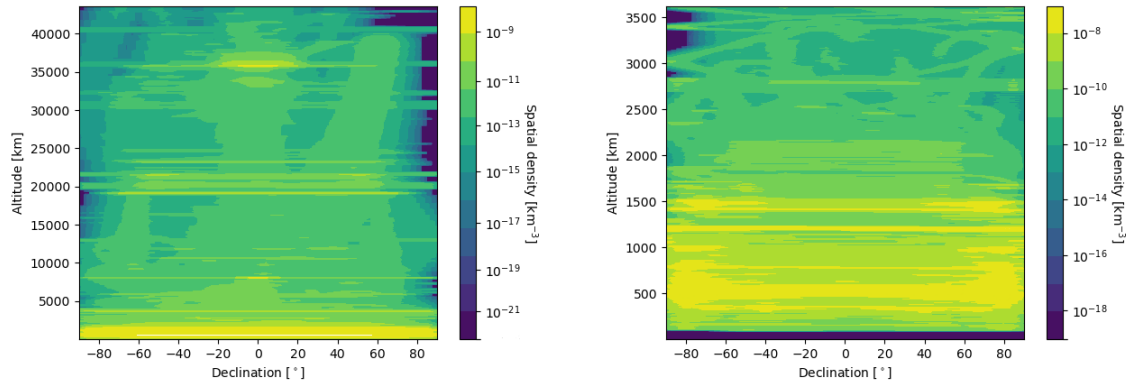


Figure 4.16: Density of operational satellites for different declinations and altitudes. The figure to the right is a zoomed view of LEO. Note that the colour bar is in log scale.

4.3 Risk Assessment Results

Simulating a spacecraft in an equatorial orbit and calculating the collision risk for different eccentricities and semi-major axes using the spatial densities obtained, one arrives at Figure 4.17.

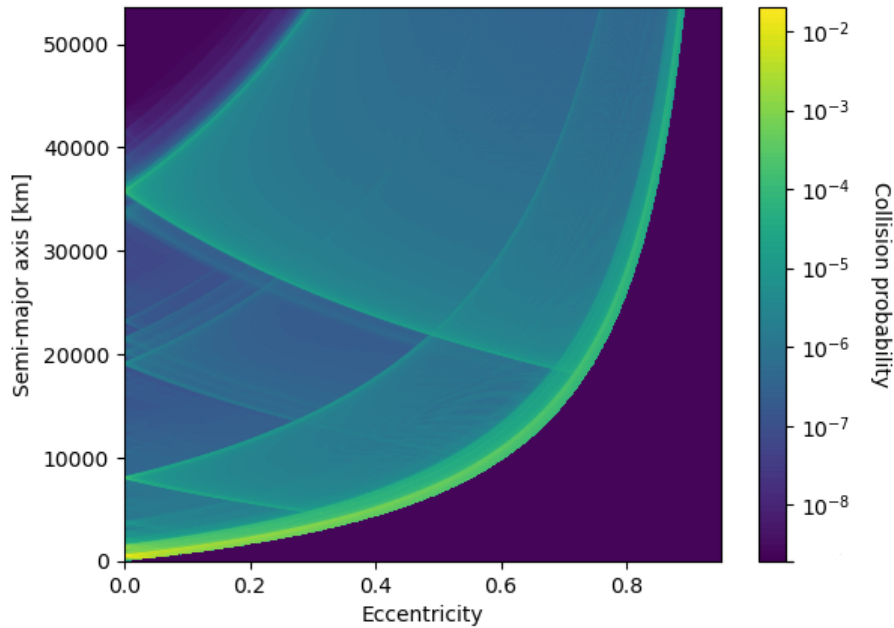


Figure 4.17: Collision probability of a spacecraft with another functioning spacecraft with the orbital parameters shown in the axes, an inclination of 0° , and a cross-sectional area of 75 m^2 , for a mission duration of 14 years (assuming constant density). Note that the colour bar is in log scale.

Using the fluxes obtained from the spatial densities, the collision probability can be obtained. Defining a spacecraft with an area of 75 m^2 , with a mission duration of 10 years, the values in Table 4.2 is obtained.

Table 4.2: 10 year collision probabilities for the orbits specified in Table 3.2, using a spatial density containing debris larger than 1, 5, and 10 cm, for a spacecraft with a surface area of 75 m², using the analytical and simulated impact velocity model. The ratio between the model value and the MASTER value is also provided to facilitate comparisons.

Orbit # > 1 cm	Model Prob. (analytical)	Model Prob. (simulated)	MASTER Prob.	Ratio (analytical)	Ratio (simulated)
1	29.96%	17.19%	22.10%	1.36	0.78
2	0.0854%	0.0577%	0.0241%	3.54	2.39
3	4.520%	3.761%	4.352%	1.04	0.86
4	0.1310%	0.0826%	0.0966%	1.35	0.85
> 5 cm					
1	4.680%	2.562%	3.458%	1.35	0.74
2	0.0071%	0.0043%	0.0015%	4.78	2.93
3	0.4494%	0.3805%	0.4246%	1.05	0.90
4	0.0078%	0.0049%	0.0060%	1.30	0.81
> 10 cm					
1	2.390%	1.290%	1.779%	1.34	0.73
2	0.0037%	0.0021%	0.0006%	6.23	3.64
3	0.2327%	0.1994%	0.2222%	1.05	0.90
4	0.0030%	0.0019%	0.0023%	1.30	0.81

This analysis shows that there is a consistent difference between the models for different spatial densities. Larger and more distant object seem to have a larger relative difference with the MASTER model. However, it is important to note that all of the orbits, for all of the densities, are similar. Typically the risks do not differ by more than a percentage point. Since neither the implemented model, nor MASTER are precise it can be determined that the model is of comparable in its area of use to MASTER.

4.4 Obtaining the Results

The fragmentation and risk models can be combined into a single *integrated model*, once they are verified. The aim of this is to create a model capable of accurately simulating a breakup event and, using the results from this, calculate a general risk increase due to this breakup. The model can now be used for a variety of purposes, specifically analysing fragmentations and the risk following these. For instance, it is impossible to be certain that all of the fragments following a fragmentation are observed. With this model the fragmentation can be simulated, and using the risk analysis model it can be determined how important it is to continue searching for pieces of debris. In this thesis, the integrated model will be used to study two different scenarios.

For the first scenario, the orbit that has the biggest effect on the general satellite population if a satellite in this orbit were to fragment will be studied. This is a problem with six independent variables; the Keplerian elements of the fragmenting satellite. However, due to the assumption that the spatial density is longitudinally symmetric, the RAAN does not need to be considered. By disregarding the RAAN,

the problem is reduced down to five independent variables. Now it is possible to iterate over the ranges of all variables and find the combination which gives the largest collision risk for an explosion. The reason for considering an explosion instead of a collision is because there is no collision vector without a colliding satellite. By adding a colliding satellite the problem would increase by the amount variables needed to simulate the colliding satellite, including: velocity (direction and magnitude), and mass. This would drastically increase computation time, likely without significantly changing the final probability. As such only explosions will be considered for this specific analysis. To perform this analysis the ranges of values in Table 4.3 will be used.

Table 4.3: Variables and their ranges used for the fragmentation and collision risk test. The notations used are the same as in Section 2.1.1.

Parameter	Range
e	$[0, 0.9]$
a (km)	$[6400, 45000]$
i ($^\circ$)	$[0, 180]$
ω ($^\circ$)	$[0, 180]$
ν ($^\circ$)	$[0, 180]$

These values are chosen such that as much as possible of the Earth orbital domain used by satellites is covered. The eccentricity is limited by 0.9 to allow the debris to extend further without being on an escape trajectory. The inclination is limited to below 180° to speed up the calculations. Performing the calculations with the full 360° range would not affect the end results significantly since an inclination of 270° is equivalent to an inclination of 90° , just rotated 180° in the longitudinal direction, which by previous assumptions is disregarded.

Once the explosion is simulated, each fragment can be propagated, and the corresponding collision risk, P_i , can be found. Once the individual risk for each fragment is found the compound collision risk can be calculated using each fragment's complementary probability. This is done by considering the probability that none of the fragments collide, and then finding its complementary. This gives the probability that at least one of the fragments will collide within the given time frame:

$$P_{\text{tot}} = 1 - \prod_{i=1}^N (1 - P_i). \quad (4.7)$$

Performing this calculation for the values within the ranges defined in Table 4.3 will give the orbits where the risk following a fragmentation is the highest.

Generating the position and velocity of the satellite explosion having the potential to do the most damage is very time consuming, and as such the results from this run may not be very accurate. The test was run twice, and both times the answer converged to similar results. As such the results can be expected to be adequate, but may still be far from perfect. The tests found that an explosion situated at a latitude of roughly 48° , 6430 km from the surface with the following Keplerian parameters: $a = 9722$ km, $e = 0.32$, $i = 132^\circ$, $\omega = 261^\circ$, $\nu = -170^\circ$, would generate the highest risk of collision. The eccentric orbit causes the fragments to survive longer in orbit. The

orbit is visualized in Figure 4.18. It is important to note that these results may differ from the global maximum due to the computation times involved.

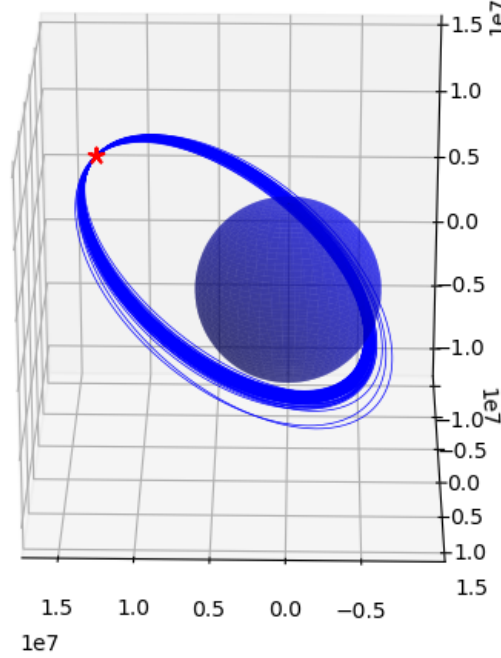


Figure 4.18: The explosion that generates the highest collision risk with other functioning satellites. The position of the explosion is marked with a red star, and the blue lines are the fragment's trajectories.

The second scenario that is studied is the NOAA-16 satellite explosion. It will be simulated for a variety of different minimum characteristic lengths to see how the significance of the debris size for the collision risk varies in this specific case. The sizes tested will be: >1 cm to >15 cm, in increments of 2 cm. This will be done by generating an explosion, and computing the collision risk for each fragment, and then combining them according to (4.7).

For reference, the risk of collision with the NOAA-16 prior to its explosion, given that its orbit stays the same, can be found after finding its average cross-sectional area. The satellite can be modelled as a cylinder with a single solar panel, with the dimensions: 4.19 m long, 1.88 m diameter, and a 2.73 m by 6.14 m rectangular solar array [37]. An estimate of the cross sectional area can be found by averaging the maximum cross sectional area, with the minimum. The maximum area is the long side of the cylinder, combined with the area of the solar array: $1.88 \times 4.19 \text{ m}^2 + 2.73 \times 6.14 \text{ m}^2 = 24.7 \text{ m}^2$. The minimum area is found when the satellite is head-on, perpendicular to the solar array. Thus, the cross sectional area is simply the area of the cylinder from the top: $\pi r^2 = 2.77 \text{ m}^2$. The average area obtained is: $\frac{1}{2}(24.7 + 2.77) \text{ m}^2 = 13.7 \text{ m}^2$. Including some margin for error this can be increased to 15 m^2 , which, after plugging this into the model, gives a 20 year collision probability of 0.019%. This value is low due to having a very high orbit, above most other LEO and SSO spacecraft. Simulating an explosion of NOAA-16 gives the results seen in Table 4.4.

Table 4.4: Collision risk of simulated debris from the NOAA-16 explosion.

Minimum characteristic length, $L_{c,\min}$ (cm)	Collision Probability (%)
1	0.33
3	0.31
5	0.30
7	0.29
9	0.29
11	0.28
13	0.27
15	0.26
No Explosion	0.019

From this it is clear that a fragmentation may drastically increase the collision risk, by at least an order of magnitude. The results also show that there is a *relative* increase of approximately 15% in collision probability when accounting for objects smaller than the typical radar resolution of around 10 cm. It is important to note that these simulations are based on randomly generated values from various distributions, and as such the probabilities varies between runs. However, between several tests the maximum probability consistently stayed between 0.3%–0.4%.

In particular, some intervals may be more interesting than others. For instance the debris can be grouped by detection probability, where fragments 10 cm or larger are very likely to be detected, 7–10 cm are less likely to be detected, but can possibly be detected, and 1–7 cm which are very unlikely to be detected. Given these intervals the collision probabilities are shown in Table 4.5.

Table 4.5: Collision risk of simulated debris from the NOAA-16 explosion, divided into groups based on detection probability.

Characteristic length, $L_{c,\min}$ (cm)	Collision Probability (%)
1–7	0.04
7–10	0.01
> 10	0.28
Cumulative:	0.33

Chapter 5

Discussion

This chapter presents a detailed discussion of the results obtained from the analysis of NASA's Standard Breakup Model (SBM) for various fragmentation events in space. The discussion will focus on the observed discrepancies between simulations and the actual events, highlighting the limitations of the model and its potential applications for future studies. By examining the behavior of the model and the accuracy of its simulations for different scenarios, this section aims to provide insights into the underlying factors that affect the effectiveness of the SBM, and to explore possible solutions to improve its performance. Following this, the risk model's accuracy is validated through a comparative study with a known accurate model for similar scenarios. The spatial density and risk model is also validated by simulating a spacecraft in different equatorial orbits, which reveals the effect of constellations at different orbits on the collision risk. Finally, two scenarios will be studied to demonstrate the practical applications of the integrated model.

5.1 Breakup Model

Given the importance of the Gabbard diagram as an initial analytical tool for assessing fragmentations, it can be beneficial to compare the Gabbard diagram of a simulated fragmentation with that of actual events. These comparisons serves various purposes, including verifying the fragmentation position and indirectly determining the time of fragmentation. In the case of the Delta upper stage explosion, Figure 4.1 indicates that the observed fragments exhibit a spread ranging from 500 to 2500 km, which is consistent with the model's predictions. The model has some additional spread, primarily resulting from edge cases generated due to the model's stochastic nature. The central point on the diagram represents the fragmentation altitude, which is consistent for both cases.

The Gabbard diagram for the NOAA-16 explosion, Figure 4.5, presents an interesting observation: the spread of fragments in the simulated scenario slightly exceeds that of the observed case. The observed fragments indicates a general spread of 700 to 1100 km, while the simulated diagram depicts a general range of 600 to 1200 km, an excess of approximately 100 km in each direction. This corresponds to an error of approximately ± 25 m/s in the downrange direction for fragments within the excess range.

In the case of the Iridium–Cosmos collision, the Gabbard diagrams reveal certain discrepancies, which will be discussed in more detail later. However, the main insights from the diagrams are two-fold. Firstly, the simulated Gabbard diagram for the Iridium-33 satellite does not align well with the observed diagram. Secondly, numerous observed fragments from the Cosmos-2251 exhibit significant perturbations caused by drag. Regardless, it can be seen that the Cosmos-2251 simulation better corresponds to the observed data than the Iridium-33 simulation. This conclusion is supported by examining the range of Cosmos-2251 fragments, where the observed data spans from 200 to 1600 km, which is consistent with the simulated data range. The dissimilarity in appearance is primarily attributed to drag-induced perturbations. The simulated fragments extend into the atmosphere and reach up to approximately 1600 km, with a few fragments found beyond that threshold, similar to the observed fragments.

In terms of quantitative results, the implementation of the breakup model shows a behavior similar to other implementations of NASA’s SBM. Notably, it is clear that it simulates some types fragmentation events more accurately than others. For instance, the explosion of the NOAA-16 satellite is relatively well-represented, while the Iridium–Cosmos collision shows some deviations from the observed values, especially for the Iridium-33 satellite. This can be attributed to the fact that the SBM is based on observations predating the collision, and as such the data that supports it is not included. Modern satellites typically use lightweight composite materials, which result in higher area-to-mass ratios (A/M), which are not fully accounted for in the model. Additionally, older satellites have a higher fragmentation rate, due to aged hardware and non-implemented policies, such as discharging the batteries when a satellite is put out of service. This further skews the model’s bias towards older satellites. Consequently, the A/M ratio of more recent satellites is often underestimated in the SBM, which in turn affects the fragment velocities, as seen in the case for Iridium-33. Cosmos-2251 is less affected by this due to its satellite bus being manufactured with older materials [10, 38].

Moreover, as previously discussed, the Gabbard diagram for the NOAA-16 event exhibits a discrepancy which corresponds to an error of up to 25 m/s in the downrange direction, for some fragments. This inconsistency is apparent in both Figures 4.6 and 4.7. The simulated fragments disperse isotropically as intended, conforming to the implemented model. However, the observed fragments appear slightly compressed in the downrange direction, which can be seen in the data in Figure 4.6. This compression could be attributed to the origin of the explosion or potential non-uniformity within the battery. Nevertheless, it is important to note that it introduces only a minor deviation in the overall velocity perturbations. Consequently, its impact on future risk assessments is expected to be negligible. The mean simulated Δv is comparable to the observed, differing by only 7 m/s.

Another noteworthy result is that the number of fragments obtained from the simulations differs substantially from the observed values in some scenarios. This discrepancy can be attributed to various factors, including the year of fragmentation which affects the resolution of the radar equipment used to detect the fragments. For instance, the Delta upper stage explosion, which occurred early in the space age when radar equipment had lower resolution, is overestimated in the model in terms of the number of fragments. This is expected since the resolution used to simulate the

explosion was higher than that of the time.

On the other hand, the Iridium–Cosmos collision shows a significant difference in the number of fragments detected compared to the observed values, even though it happened recently. To minimize errors due to perturbations, this report considers only fragments discovered within 6 months, whereas, in total, over 600 fragments were discovered for the Iridium-33 satellite and over 1600 for the Cosmos-2251 satellite [1]. The increased resolution of modern radar equipment used to detect these fragments could be one possible explanation for this discrepancy. Furthermore, the relatively low orbit of the collision also contributes to a higher number of visible fragments. Simulating the collision using a resolution of 6–7 cm provides comparable values for the number of debris generated for each satellite.

The problem that arises when comparing Δv 's for histograms with different amounts of fragments can be circumvented by normalizing them. This is done in Figures 4.4 and 4.8, which shows that the Delta upper stage explosion is very well represented when considering it as an isotropic explosion. The same can be said about the NOAA-16 histogram, which also shows a good correspondence between the data and the model.

One distinguishing feature with the fragment velocity model is the accuracy with which it simulates the direction of the velocities. The results from both the explosion cases (Figures 4.2 and 4.6), and the collision case (Figure 4.10) shows that the model accurately simulates the spread of fragments in the correct directions, with one exception being the Cosmos-2251 satellite. The simulation results matches the expected results based on the direction of the collision, shown in Figure 4.14, but the data presents some interesting features.

The Cosmos-2251's dv_x vs dv_r plot (Figure 4.14) does not show much similarity between the simulated and observed results, most likely due to perturbations affecting many of the fragments between the time of collision and time of observation. These perturbed fragments lie on the horizontal line that is visible, which appears due to the equations governing the velocity perturbations not having a real solution. This was discussed in Section 2.1.3, but can be avoided by observing the fragments sooner or disregarding these fragments.

Focusing on the Iridium-33 fragments, Figures 4.11 and 4.12, shows that the spread of fragments in the simulated case is still slightly too high, which indicates that the standard deviation of the rotations can be lowered even further. This can be tuned by simulating multiple collisions and finding the optimal value. The normalized histogram also suggest that the SBM still has room for improvement. As previously mentioned, the satellite is made of lightweight materials. The consequence of this is that the area-to-mass ratio increases. According to (2.54) this increase in A/M would lead to *higher* ejection velocities, but the SBM, which generates area-to-mass ratios that are roughly three times higher than the observed (for Iridium-33) [38], still overestimates the velocities by more than double. This suggests that the area-to-mass ratio needs to *decrease* to lower the velocities, which would even further increase the gap between the area-to-mass ratios. This shows that the SBM is consistent in modeling older spacecraft, but has room for improvement regarding more modern materials.

Nevertheless, the consistency between the other velocity histograms demonstrates the

accuracy of the model in simulating fragmentations of this type. The examined collision has exhibited some deviations, most likely due to problems with the SBM itself, but the spread of fragments in all cases behave as expected. It becomes more obvious that many of the deviations experienced between the model and simulation arise from the SBM since the mean total Δv , which is independent of rotation, does not always match the observed case, which can be seen for example in Iridium-33. To correct this the SBM itself has to be modified, which may be difficult due to the difficulty of obtaining empirical data.

5.2 Risk Model

The validation of the spatial density and risk model is accomplished through a comparative study with a known accurate model. Table 4.1 presents the obtained fluxes for different orbits. The probabilities, which are obtained by converting the fluxes using (2.38), provides a more intuitive way of comparing the model with MASTER. These probabilities are shown in Table 4.2. This reveals varying accuracies for the different orbits, with some orbits being more similar to MASTER than others. For instance, comparing the collision probabilities for orbits 2 and 3 reveals a considerable difference in the relative difference between the models. One possible reason is that sparser regions will in general have lower fluxes, which results in lower collision probabilities. This amplifies the impact of numerical errors due to the small probabilities that are involved. If one instead examines the absolute difference, it is evident that the models are quite similar for the orbits located in sparser regions, orbits 2 and 4.

A possible reason for the differences can be seen in Tables 4.1 and 4.2. These suggest that the impact velocity model may have a significant effect on the collision probability. In general, the MASTER probability lies in-between the two impact velocity models used, but based on the difference to the MASTER results it seems like the analytical model is worse than the simulated model for the larger orbits. For the orbits with smaller errors, both models have a similar difference relative to the MASTER model. Interestingly, this difference is in opposite directions. The simulated impact velocity model underestimates the flux, whereas the analytical model overestimates the flux. Regardless, since both models are approximations based on gas theory, there is no definitive correct answer. The fact that both models in general agree with each other on the collision probability is noteworthy.

Nonetheless, the differences between the models may also be explained by various other functionalities that may be implemented in the MASTER model, such as time-varying spatial densities, as well as different models that may be used to calculate different parameters. In general, even due to these differences, the implemented model and MASTER behave very similar to each other, and the results shows that a more fine-tuned velocity impact model may further increase the similarities.

The spatial density and risk model is also validated by simulating a spacecraft in different equatorial orbits, as shown in Figure 4.17. This figure displays the expected effect the constellations at different orbits have on the collision risk, with the visible curves or boundaries representing the intersection of the satellite's orbit with the orbits of a specific constellation. These boundaries' shape can be determined by solving for the semi-major axis, a , as a function of the eccentricity, e , in (2.3) and (2.4). Figure 4.17

shows that the different constellations are correctly represented in the spatial density model, and the risk model accurately accounts for them by providing a higher collision probability in denser regions, even for the generated spatial density, not just for the MASTER-obtained density.

5.3 Combined Model

The integration of both models to evaluate risk subsequent to satellite fragmentation was tested for two scenarios. The first scenario, which aimed to identify the explosion that poses the highest subsequent risk, yielded mostly inconclusive results due to long computation times rather than the model itself. Nevertheless, the orbit found may still be detrimental to the orbital domain. It not only passes through the denser parts of the SSO and LEO regions but, because of the eccentricity, it does so with a high speed which, according to (2.38), increases the collision risk.

On the other hand, the second scenario demonstrates the advantages of the model. It not only returned the expected number of fragments, facilitating the identification of undetected fragments and if any necessary allocation of additional resources for their discovery is needed, but also provided insight into the significance of smaller fragments in the post-fragmentation risk assessment. The study of NOAA-16 exemplifies this as it confirms that the expected and observed numbers of fragments for a resolution of approximately 10 cm are similar. This can then be used to calculate the risk, as presented in Table 4.4, which indicates that smaller fragments contribute to a relative increase of approximately 15% from the 10 cm risk. However, all of these fragments cannot necessarily be observed. Table 4.5 shows that the smaller, observable fragments account for a much smaller relative increase of only 3%. This can then be used to help determine if the difference in risk caused by fragments below different sizes requires additional measures to be taken to detect the remaining fragments.

It is important to note that the aforementioned collision probabilities are only for general cumulative collisions, and the risk of close encounters that necessitate evasive action will be higher. The relatively low values are explained by the fact that NOAA-16 was in a relatively sparse orbit, above most LEO and SSO satellites. Since the probabilities also do not account for orbital decay or new launches within those 20 years that the risk is calculated for, the collision probability will remain low. Additionally, one may assume that the collision probability for the fragments generated that are smaller than 10 cm would be significantly higher than the fragments that are larger than 10 cm, since there are many more small fragments. Intuitively, this makes sense. However, using the gas theory approximation, one is left with a model that depends on the area of each fragment and its orbit. As the larger fragments contribute significantly more to the total area of the fragments, they account for a larger collision probability.

These validations and examples demonstrate that the implemented model can be used to determine an estimated risk following a fragmentation. It also demonstrates that it is possible to aid in the analyses of fragmentations by plotting them on the Gabbard diagrams and simulating the results, which allows for a more accurate determination of the cause. By changing the spatial density that is used to, for example, a spatial density containing the satellites in a constellation, one can obtain the risk specific for that constellation. This can be useful for risk assessment, but can also help determine

the impact that the constellation has on the space environment by comparing it to the total risk.

The scenarios highlighted are only two of many possible scenarios that the model can be used for. Some possible scenarios where it can be used are:

- Use it to model the spread of debris following a fragmentation, to facilitate detection.
- Evaluate orbits based on the collision risk, and risk resulting from a possible or fragmentation.
- Determine the impact a future unavoidable fragmentation event may have on the space environment.
- Model the risk caused by satellite constellations, or other large groups of objects.
- Evaluate fragmentations to, for instance, see if all of the fragments are detected, determine possible cause, and facilitate identification.

All of these results are built on the assumption that the densities are longitudinally symmetric, but this is not necessarily the case. Of course, for LEO and very long durations this assumption holds, but for geostationary orbits this is not the case. In geostationary orbits the satellites are less spread out, and are often situated in groups over largely populated areas such as North America and Europe. Areas that are less populated, such as above the Pacific, contains fewer geostationary satellites. Since the longitude of these satellites are constant, this approximation does not hold. Another issue with the combined model is that the fragmentation is stochastic, meaning that each time a fragmentation is simulated, slightly different results are obtained. Combining this with the collision model means that the collision risk varies between runs. This can be somewhat mitigated by averaging the percentages over several runs, but is still something to have in mind.

Chapter 6

Conclusion

The risk analysis study that has been conducted demonstrates the ability to model satellite and rocket body fragmentations, and using the results from this to calculate a general long-term collision risk with respect to a satellite population. This allows for more in-depth analyses of fragmentations, such as the ability to study the risk caused by fragments that are too small to be observed.

The implementation of the Standard Breakup Model (SBM) behaves similar to the original implementation of NASA's SBM, but it simulates some fragmentation events better than the original breakup model by estimating the directions of the fragments. This makes it possible to simulate collisions and determine how the distribution of fragments evolves. The performance of the model is affected by factors such as the materials used in the construction of the satellite.

One of the key limitations of the SBM is its inability to fully account for materials used in modern satellites. This results in a general underestimation of the area-to-mass ratios, which in turn affects the fragment velocities. This introduces a bias towards older satellites which may negatively affect the predictions of more modern satellite fragmentations. Consequently, this also makes it more accurate when modeling the fragmentations of older satellites. The number of fragments obtained from the simulations differ from the observed values in some scenarios, highlighting the influence of the resolution of the radar equipment used to detect the fragments. Despite its limitations, this implementation of the SBM can simulate the directionality of fragment velocities, which is highlighted by the results for both the explosions and collisions. These results show that the model generates reasonable velocity distributions for different fragmentation events.

The accuracy of the risk model is validated through a comparative study with a known model for similar scenarios. This shows that the collision risk is calculated correctly and that it can be applied to a general spatial density. This thesis also introduces a method of obtaining the spatial density of a satellite population, which makes it possible to use the generated model to evaluate the risks for specific satellites.

In conclusion, the implementation of the fragmentation risk model provides a useful tool to study fragmentation events in space. However, the limitations of the model need to be carefully considered when interpreting its predictions. The integration of the fragmentation and risk models can provide insights into the collision risks associated

with specific scenarios, making it a valuable tool for space debris mitigation efforts. Further studies can improve the accuracy of the models, taking into account the limitations and uncertainties involved in the prediction of fragmentation events and collision risks in space.

6.1 Future Work

This thesis has built the groundwork for a satellite fragmentation and risk analysis model, but there are some limitations of the model that can be improved upon. Notably, a material dependence can be implemented such that the area-to-mass ratio distribution matches for satellite fragmentations involving more modern materials. Additionally, orbital decay and future launches can be implemented in the risk analysis model. This would allow for a more accurate computation of collision risk, and allow the debris to decay through orbital shells.

An interesting study that can be performed is to compare how the gas theory approximation used to calculate collision probability differs from other, more analytical models, as well as fine-tune the impact velocity model to more accurately fit other models such as MASTER. Similarly, the accuracy of disregarding the longitudinal axis can be investigated for shorter time frames to see if it can be used to speed up computations.

The model is implemented solely in a code format, and as such it is not very user-friendly. Work can be done to create a user interface to increase usability. This would facilitate how the model is used, and make it easier to change parameters and analyse the consequences of fragmentation events.

The Standard Breakup Model is used by many institutions and, as such, much research has been done on how it can be improved. The implementation presented in this thesis is based on the original NASA Evolve 4.0 implementation. However, articles such as [39] and [31] suggest various improvements that can be implemented in order to improve the accuracy of the model, especially for various edge cases such as when generating velocities for larger fragments.

Finally, the model can be used as a tool to facilitate the research and evaluation of satellite fragmentations. For instance, it can be used as an aid to determine the direction of impact of an ASAT or a satellite collision, but it can also be used to analyze the risks associated with them.

Bibliography

- [1] A. Tan and R.C. Reynolds. *Theory of satellite fragmentation in orbit*. World Scientific, 2020. ISBN: 9789811208553.
- [2] D.J. Kessler, N.L. Johnson, J.-C. Liou, and M. Matney. “The Kessler Syndrome: Implications to Future Space operations”. In: *Advances in the Astronautical Sciences* (2010).
- [3] *ESA’s Annual Space Environment Report*. Apr. 2022.
- [4] T. Sundberg and H. Sundberg. *Rymdskrot – nulägesbeskrivning, potentiell utveckling och aktuella forskningsfrågor*. FOI Memo 7580. 2021.
- [5] V. Braun, S. Lemmens, H. Krag, and Q. Funke. “Analysis of Breakup Events, 7th European Conference on Space Debris”. In: vol. 7. ESA Space Debris Office, 2017.
- [6] *Anti-satellite weapons, countermeasures, and Arms Control*. Congress of the U.S., Office of Technology Assessment, 1985.
- [7] L. Grego. *A History of ASAT Programs, Union of Concerned Scientists*. Jan. 2012. URL: https://www.ucsusa.org/sites/default/files/2019-09/a-history-of-ASAT-programs_lo-res.pdf (visited on 01/30/2023).
- [8] A.J. Tellis. *India’s ASAT test: An incomplete success*. Apr. 2019. URL: <https://carnegieendowment.org/2019/04/15/india-s-asat-test-incomplete-success-pub-78884> (visited on 01/30/2023).
- [9] *ESA’s Fragmentation event database statistics*. URL: <https://fragmentation.esoc.esa.int/home/statistics> (visited on 02/03/2023).
- [10] N. Cimmino, G. Isoletta, R. Opromolla, G. Fasano, A. Basile, A. Romano, M. Peroni, A. Panico, and A. Cecchini. “Tuning of NASA standard breakup model for fragmentation events modelling”. In: *Aerospace* 8.7 (2021). DOI: 10.3390/aerospace8070185.
- [11] W. Joubert and S. Tingay. “Simulations of orbital debris clouds due to breakup events and their characterisation using the Murchison Widefield Array Radio Telescope”. In: *Experimental Astronomy* 51 (2020). DOI: <https://doi.org/10.1007/s10686-020-09684-7>.
- [12] A. Tan and M. Dokhanian. “Velocity Perturbations Analysis of the Fengyun-1C Satellite Fragmentation Event”. In: *Advances in Aerospace Science and Applications* (2013). ISSN: 2277-3223.

- [13] N.L. Johnson, P.H. Krisko, J.-C. Liou, and P.D. Anz-Meador. “NASA’s new breakup model of Evolve 4.0”. In: *Advances in Space Research* 28.9 (2001). DOI: 10.1016/s0273-1177(01)00423-9.
- [14] B. Tingley. “2 big pieces of space junk nearly collide in orbital ’bad neighborhood’”. In: *Space.com* (Jan. 2023). URL: <https://www.space.com/space-debris-near-miss-orbital-bad-neighborhood> (visited on 01/31/2023).
- [15] *Space situational awareness*. URL: https://www.spacefoundation.org/space_brief/space-situational-awareness/ (visited on 01/31/2023).
- [16] *Space-Track.org*. URL: <https://www.space-track.org/> (visited on 01/31/2023).
- [17] B.D. Tapley. *Statistical orbit determination*. eng. Elsevier Academic Press, 2004. ISBN: 1-281-01893-7.
- [18] D.A. Vallado. *Fundamentals of Astrodynamics and Applications*. Microcosm Press, 2003. ISBN: 978-1881883180.
- [19] W.K. Tobiska, R. Culp, and C. Barth. “Predicted solar cycle twenty-two 10.7 cm flux and satellite orbit decay”. In: *Journal of The Astronautical Sciences* 35 (1987).
- [20] B.F. Chao. “Earth’s Oblateness and its Temporal Variations”. In: *Comptes Rendus Geoscience* (2006). La Terre observée depuis l’espace. ISSN: 1631-0713. DOI: <https://doi.org/10.1016/j.crte.2006.09.014>.
- [21] B. Hofmann-Wellenhof, H. Lichtenegger, and E. Wasle. *GNSS - Global Navigation satellite systems: GPS, GLONASS, Galileo, and more*. Springer, 2008. ISBN: 978-3-211-73012-6.
- [22] G.E. Cook. “Perturbations of Satellite Orbits by Tesseral Harmonics in the Earth’s Gravitational Potential”. In: *Planetary and Space Science* (1963). ISSN: 0032-0633. DOI: [https://doi.org/10.1016/0032-0633\(63\)90192-2](https://doi.org/10.1016/0032-0633(63)90192-2). URL: <https://www.sciencedirect.com/science/article/pii/0032063363901922>.
- [23] N.L. Johnson, E. Stansbery, D.O. Whitlock, K.J. Abercromby, and D. Shoots. *History of on-orbit satellite fragmentations (14th edition)*. NASA, 2008.
- [24] G. Neuneck. “China’s ASAT test — A warning shot or the beginning of an arms race in space?” In: *Yearbook on Space Policy 2006/2007: New Impetus for Europe*. Ed. by K. Schrogl, C. Mathieu, and N. Peter. Vienna: Springer Vienna, 2008, pp. 211–224. ISBN: 978-3-211-78923-0. DOI: 10.1007/978-3-211-78923-0_9.
- [25] M.J. Matney. “Algorithms for the computation of debris risk”. In: *NASA Orbital Debris Program Office* (2017).
- [26] D.J. Kessler. “Derivation of the collision probability between orbiting objects: the lifetimes of Jupiter’s outer moons”. In: *Icarus* 48.1 (1981), pp. 39–48. ISSN: 0019-1035. DOI: [https://doi.org/10.1016/0019-1035\(81\)90151-2](https://doi.org/10.1016/0019-1035(81)90151-2). URL: <https://www.sciencedirect.com/science/article/pii/0019103581901512>.
- [27] D.S. McKnight and F.R. Di Pentino. “New insights on the orbital debris collision hazard at GEO”. In: *Acta Astronautica* 85 (2013), pp. 73–82. ISSN: 0094-5765. DOI: <https://doi.org/10.1016/j.actaastro.2012.12.006>. URL: <https://www.sciencedirect.com/science/article/pii/S0094576512004869>.

-
- [28] *space debris user portal*. URL: <https://sdup.esoc.esa.int/> (visited on 02/14/2023).
 - [29] D.J. Kessler. “Orbital debris environment for spacecraft in low earth orbit”. In: *Journal of Spacecraft and Rockets* 28.3 (1991), pp. 347–351. DOI: 10.2514/3.26250. URL: <https://doi.org/10.2514/3.26250>.
 - [30] *Enhancement of S/C Fragmentation and Environment Evolution Models*. Institute of Space Systems (IRAS). Aug. 26, 2020.
 - [31] S. Frey and C. Colombo. “Transformation of Satellite Breakup Distribution for Probabilistic Orbital Collision Hazard Analysis”. In: *Journal of Guidance, Control, and Dynamics* 44.1 (2021), pp. 88–105. DOI: 10.2514/1.G004939.
 - [32] *Recent developments in space debris environment modelling, verification and validation with MASTER*. URL: <https://conference.sdo.esoc.esa.int/proceedings/sdc8/paper/28> (visited on 02/14/2023).
 - [33] J.-C. Liou, N.L. Johnson, P.H. Krisko, and P.D. Anz-Meador. “The new NASA orbital debris breakup model”. In: *Dust in the Solar System and other Planetary Systems*. Ed. by S.F. Green, I.P. Williams, J.A.M. McDonnell, and N. McBride. Vol. 15. COSPAR Colloquia Series. Pergamon, 2002, pp. 363–367. DOI: [https://doi.org/10.1016/S0964-2749\(02\)80367-5](https://doi.org/10.1016/S0964-2749(02)80367-5).
 - [34] G. Stansbery, M. Matney, J. Liou, and D. Whitlock. “A Comparison of Catastrophic On-Orbit Collisions”. In: *Advanced Maui Optical and Space Surveillance Technologies Conference*. Ed. by C. Paxson, H. Snell, J. Griffin, K. Kraemer, S. Price, M. Kendra, and D. %P. E37 Mizuno. Jan. 2008.
 - [35] A. Bade, A. Jackson, R.C. Reynolds, P. Eichler, P. Krisko, M. Matneyi, P. Anz-Meador, and N.L. Johnson. “Breakup model update at nasa/jsc”. In: (Jan. 2000), pp. 125–138.
 - [36] E. Ausay, A. Cornejo, A. Horn, K. Palma, T. Sato, B. Blake, F. Pistella, C. Boyle, N. Todd, J. Zimmerman, N. Fitz-Coy, J. Liou, M. Sorge, T. Huynh, J. Opiela, P. Krisko, and H. Cowardin. “A Comparison of the SOCIT and DebrisSat Experiments”. In: *7th European Conference on Space Debris* (Jan. 2017). ESA Space Debris Office.
 - [37] *NOAA POES Series - 5th Generation*. June 2012. URL: <https://www.eoportal.org/satellite-missions/noaa-poes-series-5th-generation#performance-specifications> (visited on 04/27/2023).
 - [38] P. D. Anz-Meador and J.-C. Liou. *Analysis and Consequences of the Iridium 33-Cosmos 2251 Collision*. Tech. rep. 2010.
 - [39] M. Oswald, S. Stabroth, C. Wiedemann, P. Voersmann, P. Wegener, and H. Klinkrad. “A revised approach for modelling on-orbit fragmentations”. In: *AIAA/AAS Astrodynamics Specialist Conference and Exhibit*. 2004.
 - [40] T.S. Kelso. “Two-line element set format”. July 2022. URL: <https://celestrak.org/columns/v04n03/>.
 - [41] F.E. Harris. *Mathematics for physical science and engineering: Symbolic computing applications in Maple and Mathematica*. Elsevier, 2014.

Appendix - Contents

A Two-line elements	63
B Gravitational harmonics derivation	64
C Impact velocity parameters	67
D Standard Breakup Model parameters	68

Appendix A

Two-line elements

TLEs is a way of formatting the orbital elements of an object orbiting the Earth such that they can easily be read and used for propagation [40]. They consist of two lines with 69 characters each in the following format [16]:

$\begin{array}{cccccccc} \overbrace{1}^1 & \overbrace{25544U}^2 & \overbrace{98067A}^3 & \overbrace{08264.51782528}^4 & \overbrace{-.00002182}^5 & \overbrace{00000-0}^6 & \overbrace{-11606-4}^7 & \overbrace{0}^8 & \overbrace{2927}^9 \\ \underbrace{1}_{10} & \underbrace{25544}_{11} & \underbrace{51.6416}_{12} & \underbrace{247.4627}_{13} & \underbrace{0006703}_{14} & \underbrace{130.5360}_{15} & \underbrace{325.0288}_{16} & \underbrace{15.72125391563537}_{17} \end{array}$

Each field contains useful information about one or more orbital parameters. A short description of each field is found in Table A.1.

Table A.1: Table describing the different fields of the TLE [16].

Line 1	Description	Line 2	Description
1	Line number	10	Line number
2	Satellite catalog number, Classification	11	Satellite catalog number
3	International designator	12	Inclination [°]
4	Epoch (Time)	13	RAAN [°]
5	Ballistic coefficient	14	Eccentricity
6	Second derivative of mean motion	15	Argument of perigee [°]
7	Drag term (B^*)	16	Mean anomaly
8	Ephemeris type	17	Mean motion [revolutions per day], Revolution number at epoch, Checksum
9	Element set number, Checksum		

The main source for much of the debris data, space-track, releases the orbital data in this format.

Appendix B

Gravitational harmonics derivation

We can find the effect caused by an asymmetric central body by considering a generalised version of (2.1), which includes the inhomogeneities of the central body's mass by considering the density instead:

$$\mathbf{F} = -Gm \int_V \frac{\rho}{r^2} \hat{\mathbf{r}} dV, \quad (\text{B.1})$$

where ρ is the non-constant density of the central body. The specific potential of a field, u , is the solution to the equation:

$$\nabla u = -\mathbf{g}, \quad (\text{B.2})$$

where the gravitational field \mathbf{g} is \mathbf{F}/m . Using vector calculus the potential of a gravitational field can be found:

$$u = -G \int_V \frac{\rho}{r'} dV. \quad (\text{B.3})$$

By substituting $dV = dm/\rho$ one gets:

$$u = -G \int_V \frac{1}{r'} dm. \quad (\text{B.4})$$

We now introduce some more variables to make the derivation simpler. In (B.4) r' is the distance from the point at which we are integrating to the orbiting object. We can now introduce \mathbf{r}_Q is the vector from the central body's center of mass to the infinitesimal mass at which we are integrating, let \mathbf{r} be the vector from the center of mass of the central body to the orbiting object, let ϕ_Q be the latitude of the point, and finally let Λ be the angle between \mathbf{r}_Q and \mathbf{r} . The geometry is illustrated in Figure B.1.

Using this the following relation holds, for coordinates:

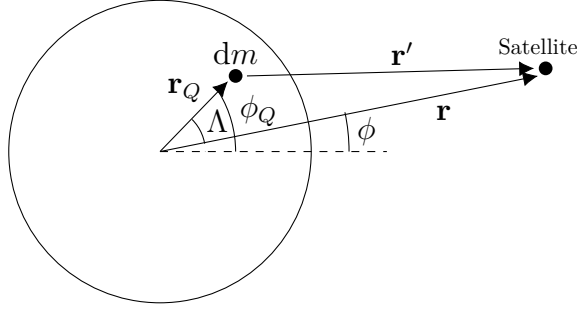


Figure B.1: Illustration of the meanings of different variables, based on Figure 8.3 in [18].

$$r = \sqrt{x^2 + y^2 + z^2}, \quad r_Q = \sqrt{\xi^2 + \eta^2 + \zeta^2}. \quad (\text{B.5})$$

where (x, y, z) , and (ξ, η, ζ) are the coordinates of the orbiting body, and the point of integration respectively. The law of cosines combined with the dot product between \mathbf{r} and \mathbf{r}_Q gives:

$$r' = r\sqrt{1 - 2\alpha \cos(\Lambda) + \alpha^2}, \quad (\text{B.6})$$

where $\alpha = r_Q/r$. Plugging this into (B.4) yields:

$$u = -G \int_V \frac{dm}{r\sqrt{1 - 2\alpha \cos(\Lambda) + \alpha^2}}. \quad (\text{B.7})$$

Since $\alpha < 1$, and $-1 \leq \cos(\Lambda) \leq 1$ it allows us to substitute $\psi = (-2\alpha \cos(\Lambda) + \alpha^2) < 1$, which gives:

$$\frac{1}{\sqrt{1 - 2\alpha \cos(\Lambda) + \alpha^2}} = \frac{1}{\sqrt{1 + \psi}} = \sum_{l=0}^{\infty} \alpha^l P_l[\cos(\Lambda)], \quad (\text{B.8})$$

where the rightmost term comes from using the binomial theorem to expand the middle term, and P_l is the l th Legendre polynomial. The l th Legendre polynomial is found using [41]:

$$P_l(x) = \frac{1}{2^l l!} \frac{d^l}{dx^l} [(x^2 - 1)^l]. \quad (\text{B.9})$$

Using the above equation, (B.7) reduces to [18]:

$$u = -\frac{G}{r} \int_V \sum_{l=0}^{\infty} \alpha^l P_l[\cos(\Lambda)] dm. \quad (\text{B.10})$$

Since Λ is very difficult to find, this equation is difficult to use in practice. Instead, one can transform the above equation to use the latitude of the orbiting object, ϕ instead. Performing this transformation and reordering one finally obtains:

$$u = -\frac{\mu}{r} \left(1 - \sum_{l=2}^{\infty} J_l \left(\frac{R_{\oplus}}{r} \right)^l P_l[\sin(\phi)] + Z(r) \right). \quad (\text{B.11})$$

The function $Z(r)$ corresponds to the *sectoral harmonics* of the central body, i.e., irregularities along the rotational axis of the central body (east-west).

Appendix C

Impact velocity parameters

The following section defines the variables used in the analytical approximation for impact/collision velocity, (2.39) [29].

$$A = 2.5 \tag{C.1}$$

$$B = \begin{cases} 0.5 & i < 60^\circ \\ 0.5 - 0.01(i - 60^\circ) & 60^\circ < i < 80^\circ \\ 0.3 & i > 80^\circ \end{cases} \tag{C.2}$$

$$C = \begin{cases} 0.0125 & i < 100^\circ \\ 0.0125 + 0.00125(i - 100^\circ) & i > 100^\circ \end{cases} \tag{C.3}$$

$$D = 1.3 - 0.01(i - 30^\circ) \tag{C.4}$$

$$E = 0.55 + 0.005(i - 30^\circ) \tag{C.5}$$

$$F = \begin{cases} 0.3 + 0.0008(i - 50^\circ)^2 & i < 50^\circ \\ 0.3 - 0.01(i - 50^\circ) & 50^\circ < i < 80^\circ \\ 0.0 & i > 80^\circ \end{cases} \tag{C.6}$$

$$G = \begin{cases} 18.7 & i < 60^\circ \\ 18.7 + 0.0289(i - 60^\circ)^3 & 60^\circ < i < 80^\circ \\ 250 & i > 80^\circ \end{cases} \tag{C.7}$$

$$H = 1.0 - 0.0000757(i - 60^\circ)^2 \tag{C.8}$$

$$v_0 = \begin{cases} 7.25 + 0.015(i - 30^\circ) & i < 60^\circ \\ 7.7 & i > 60^\circ \end{cases} \tag{C.9}$$

Appendix D

Standard Breakup Model parameters

The following section defines the variables used in the NASA Standard Breakup Model to simulate fragmentation events in orbit [13].

$$\alpha^{RB} = \begin{cases} 1 & \lambda_c \leq -1.4 \\ 1 - 0.3571(\lambda_c + 1.4) & -1.4 < \lambda_c < 0 \\ 0.5 & \lambda_c \geq 0 \end{cases} \quad (\text{D.1})$$

$$\mu_1^{RB} = \begin{cases} -0.45 & \lambda_c \leq 0.5 \\ -0.45 - 0.9(\lambda_c + 0.5) & -0.5 < \lambda_c < 0 \\ -0.9 & \lambda_c \geq 0 \end{cases} \quad (\text{D.2})$$

$$\sigma_1^{RB} = 0.55 \quad (\text{D.3})$$

$$\mu_2^{RB} = -0.9 \quad (\text{D.4})$$

$$\sigma_2^{RB} = \begin{cases} 0.28 & \lambda_c \leq -1 \\ 0.28 - 0.1636(\lambda_c + 1) & -1 < \lambda_c < 0.1 \\ 0.1 & \lambda_c \geq 0.1 \end{cases} \quad (\text{D.5})$$

$$\alpha^{SC} = \begin{cases} 0 & \lambda_c \leq -1.95 \\ 0.3 + 0.4(\lambda_c + 1.2) & -1.95 < \lambda_c < 0.55 \\ 1 & \lambda_c \geq 0 \end{cases} \quad (\text{D.6})$$

$$\mu_1^{SC} = \begin{cases} -0.6 & \lambda_c \leq -1.1 \\ -0.6 - 0.318(\lambda_c + 1.1) & -1.1 < \lambda_c < 0 \\ -0.95 & \lambda_c \geq 0 \end{cases} \quad (\text{D.7})$$

$$\sigma_1^{SC} = \begin{cases} 0.1 & \lambda_c \leq -1.3 \\ 0.1 + 0.2(\lambda_c + 1.3) & -1.3 < \lambda_c < -0.3 \\ 0.3 & \lambda_c \geq -0.3 \end{cases} \quad (\text{D.8})$$

$$\mu_2^{SC} = \begin{cases} -1.2 & \lambda_c \leq -0.7 \\ -1.2 - 1.333(\lambda_c + 0.7) & -0.7 < \lambda_c < -0.1 \\ -2 & \lambda_c \geq 0 \end{cases} \quad (\text{D.9})$$

$$\sigma_2^{SC} = \begin{cases} 0.5 & \lambda_c \leq -0.5 \\ 0.5 - (\lambda_c + 0.5) & -0.5 < \lambda_c < -0.3 \\ 0.3 & \lambda_c \geq -0.3 \end{cases} \quad (\text{D.10})$$

